J. Fluid Mech. (1999), *vol.* 393, *pp.* 175–213. Printed in the United Kingdom

An experimental investigation of a three-dimensional turbulent boundary layer in an 'S'-shaped duct

By J. M. BRUNS[1], H. H. FERNHOLZ[1] AND P. A. MONKEWITZ[2]

[1]Hermann–Föttinger–Institut für Strömungsmechanik, Technische Universität Berlin, Strasse des 17. Juni 135, 10623 Berlin, Germany

[2]Ecole Polytechnique Fédérale de Lausanne, Institut de Machines Hydrauliques et de Mécanique des Fluides, ME-Ecublens, CH-1015 Lausanne, Switzerland

(Received 28 October 1998 and in revised form 22 March 1999)

This paper describes the evolution of an incompressible turbulent boundary layer on the flat wall of an 'S'-shaped wind tunnel test section under the influence of changing streamwise and spanwise pressure gradients. The unit Reynolds number based on the mean velocity at the entrance of the test section was fixed to $10^6\,\mathrm{m}^{-1}$, resulting in Reynolds numbers Re_{δ_2}, based on the streamwise momentum thickness and the local freestream velocity, between 3.9 and 11×10^3. The particular feature of the experiment is the succession of two opposite changes of core flow direction which causes a sign change of the spanwise pressure gradient accompanied by a reversal of the spanwise velocity component near the wall, i.e. by the formation of so-called cross-over velocity profiles. The aim of the study is to provide new insight into the development of the mean and fluctuating flow field in three-dimensional pressure-driven boundary layers, in particular of the turbulence structure of the near-wall and the cross-over region.

Mean velocities, Reynolds stresses and all triple correlations were measured with a newly developed miniature triple-hot-wire probe and a near-wall hot-wire probe which could be rotated and traversed through the test plate. Skin friction measurements were mostly performed with a wall hot-wire probe. The data from single normal wires extend over wall distances of $y^+ \gtrsim 3$ (in wall units), while the triple-wire probe covers the range $y^+ \gtrsim 30$. The data show the behaviour of the mean flow angle near the wall to vary all the way to the wall. Then, to interpret the response of the turbulence to the pressure field, the relevant terms in the Reynolds stress transport equations are evaluated. Finally, an attempt is made to assess the departure of the Reynolds stress profiles from local equilibrium near the wall.

1. Introduction

Despite the importance of three-dimensional turbulent boundary layers (3DTBL) in internal and external flows, such as in turbomachines and over aircraft wings and fuselages, the understanding of the physics and the turbulence models for such flows are still poorly developed in comparison with two-dimensional boundary layers. The state of the art in 3DTBL research has been reviewed by Eichelbrenner (1973), Johnston (1976), Cousteix (1986), Ölçmen & Simpson (1992), Eaton (1995) and Johnston & Flack (1996).

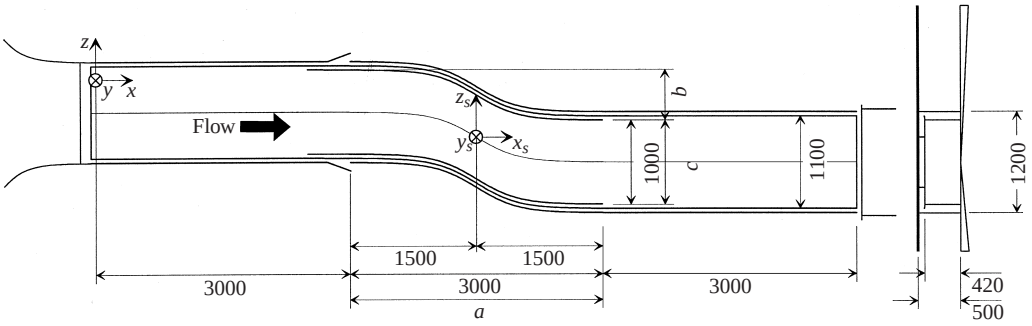

FIGURE 1. Top view and cross-section (on the right) of the 'S'-shaped wind tunnel test section. (The measuring plate is on the underside of the roof, i.e. y points into the page.) Dimensions in mm.

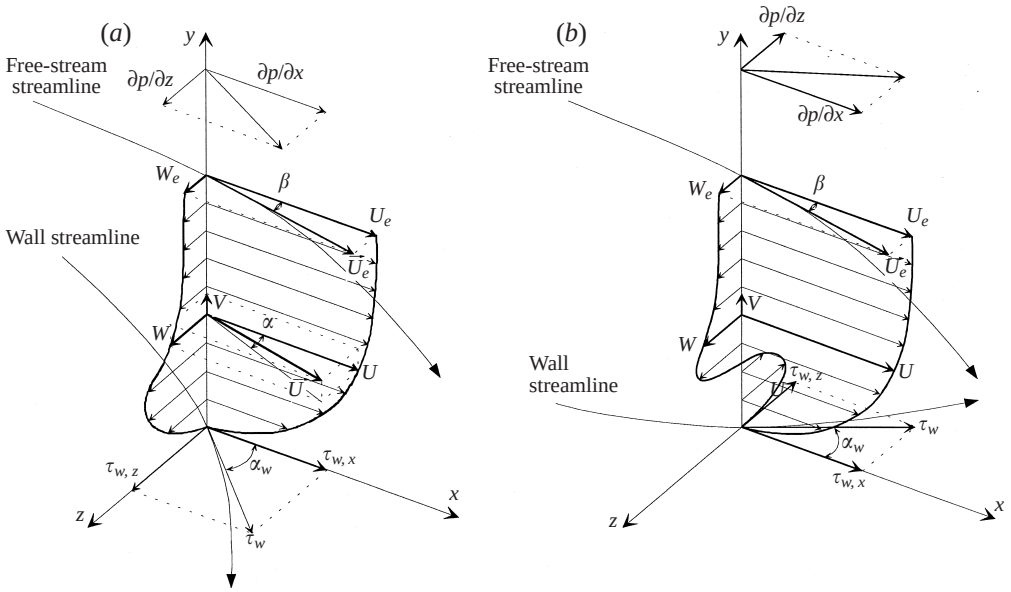

FIGURE 2. Typical pressure-driven three-dimensional boundary layer with external streamline coordinate system (ESCS): (*a*) unilaterally (*b*) bilaterally skewed.

The present experiment deals with a pressure-driven turbulent boundary layer on the flat wall of an 'S'-shaped wind tunnel test section shown on figure 1 in which the direction of the spanwise pressure gradient changes sign between the two bends of the 'S'. This causes the unilaterally skewed velocity profile at the exit of the first bend (figure 2*a*) to turn into a so-called cross-over velocity profile in which the angle of the mean flow vector relative to the free-stream direction changes sign in the low-momentum region near the wall (figure 2*b*).

The objective of this study is to investigate the development of the mean flow and of the turbulence structure in the boundary layer due to the unilateral and bilateral skewing. The emphasis is on the inner layer for which measurements are scarce or have not been available in the cross-over region. The present investigation involved measurements of mean and fluctuating velocity profiles at 33 primary and 16 secondary stations as well as the determination of static pressure and skin friction

distributions. The secondary locations were arranged around selected primary stations to evaluate the spatial derivatives arising in the Reynolds stress transport equations.

Eichelbrenner (1963) and Eichelbrenner & Peube (1966) were the first to draw attention to cross-over profiles. Klinksiek & Pierce (1970) measured mean velocity profiles with two-sided lateral skewing in an 'S'-shaped channel of rectangular cross-section and Webster, DeGraaff & Eaton (1996) in a boundary layer over a swept bump. Recent measurements were performed by Schwarz & Bradshaw (1992, 1994) and by Compton & Eaton (1995) in a curved duct with unilaterally skewed velocity profiles and by Ölçmen & Simpson (1995*b*), in the flow of a wing-body junction.

Unilaterally and bilaterally skewed velocity profiles in a relatively thick (35–90 mm) 3DTBL were generated in the 'S'-shaped wind tunnel at the Ecole Polytechnique Fédérale de Lausanne (EPFL). First results obtained in this tunnel were published by Truong & Brunet (1992) and used as a validation for numerical methods (Ryhming, Truong & Lindberg 1992). Since then, the flow uniformity in the test section has been improved, a temperature control introduced and the curvature of the sidewall of the test section increased. The objective of good near-wall measurements made it necessary to use wall hot-wire probes in addition to the surface fence for skin-friction measurements, to use miniature hot-wire probes and, above all, to develop a miniature triple-wire probe (THWP) for field measurements. The THWP permitted measurements down to $y^+ \approx 30$ while the single-wire probe, the prongs of which were traversed through the wall, yielded data down to $y^+ \approx 3$.

The only other measurements in a 3DTBL below y^+ of 40 were performed by means of LDA by Chesnakas, Simpson & Madden (1994), Ölçmen & Simpson (1995*a,b*), Chesnakas & Simpson (1996) and Compton & Eaton (1995) but their experiments did not include cross-over profiles in the sense defined above.

In the following, we describe the experimental facility and measuring techniques in § 2, the mean flow evolution in § 3 and the turbulence measurements including higher moments and space correlations at selected stations in § 4. A discussion of the local non-equilibrium of Reynolds stresses and other conclusions are finally presented in § 5.

2. Experimental facility and measuring techniques

The wind tunnel used for this experiment is the closed return tunnel with an 'S'-shaped test section of 9 m length and 1 m width at EPFL. It has an axial fan driven by a thyristor controlled 30 kW DC motor generating a maximum flow velocity of $45\,\mathrm{m\,s^{-1}}$. Temperature is controlled automatically by a custom made cooler in the flow return. It is kept constant within ± 0.1 °C at the working speed of about $16\,\mathrm{m\,s^{-1}}$ corresponding to the unit Reynolds number of $10^6\,\mathrm{m^{-1}}$ chosen for this study. Downstream of the diffuser the flow enters the settling chamber which contains a honeycomb and two precisely manufactured perforated metal plates (64% porosity, see Dengel & Fernholz 1990) to improve the flow uniformity. The nozzle, contracting in the lateral and vertical direction, has a contraction ratio 7.35:1 and is followed by a 3 m long straight part of the test section, the 'S'-shaped part and another 3 m long straight section (figure 1).

The test section (1 m wide and 0.42 m high) is a sandwich construction with the tunnel roof used as test plate. This is a polished aluminium plate with an elliptical leading edge and fitted with 1128 static pressure taps and 43 surface plugs to install wall probes. The measuring stations for this experiment are located along three lines following the curvature of the sidewalls: the centreline (M) and two lines 190 mm

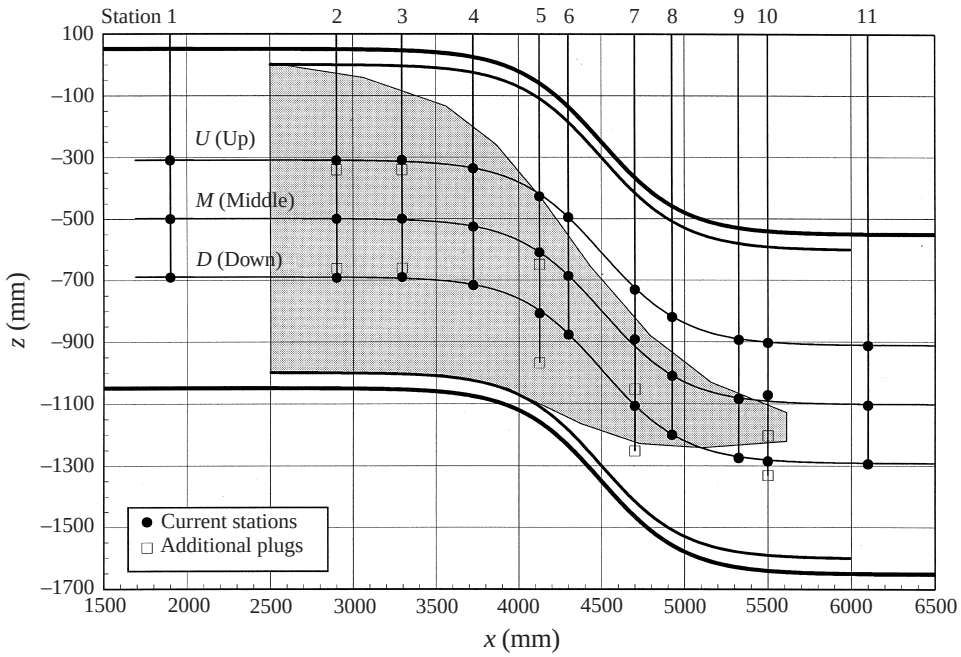

FIGURE 3. The location of measuring stations in the 'S'-shaped test section in the tunnel coordinate system (TCS). The wall-normal coordinate y points into the page.

off centre denoted (U) and (D), respectively (figure 3). The 'S'-shaped sidewalls are made of 12 mm thick cast Plexiglas, and the bottom wall consists of Plexiglas plates reinforced with plastic ribs to increase their rigidity. Slots between the plates, sealed with soft brushes, allow the traverse of the probe holder to access all measuring stations from the bottom of the test section. The boundary layers on all four walls of the test section have a defined origin since the upstream boundary layer is blown off at the inlet of the test section. For reference, the shaded area on this figure 3 represents the region accessible to a boundary-layer computation started exclusively with upstream boundary conditions (Parker 1994 and Parker & Bruns 1996). Outside the shaded region, some of the near-wall fluid originates from the sidewalls.

The main traversing system with five degrees of freedom (three translations plus probe yaw and roll) was mounted on steel rails underneath the tunnel and extended into the test section through the slots of its bottom wall. The gooseneck probe holder was positioned by five stepper motors (Micro-Control) combined with a control unit (Micro-Control IP 28). The pitch angle had to be adjusted manually. The wall probes mounted in the plugs of the test plate could be yawed and traversed perpendicular to the wall, also under computer control (see e.g. Rogers & Head 1969). For a more detailed description of the wind tunnel and the traversing system the reader is referred to Truong & Brunet (1992) and to Bruns (1998).

Special care has been taken to achieve a good flow quality in the straight upstream part of the test section. At the streamwise position $x = 1900$ mm the mean velocity distribution $\bar{u}$ across the tunnel width is constant within $\pm 1\%$ and the skin-friction distribution varies less than $\pm 2\%$. This uniform skin-friction distribution was obtained by tripping the boundary layer by means of a 3 mm high 'Velcro' strip at a distance of 100 mm from the leading edge. The free-stream turbulence level is approximately 0.2% over a frequency range 0–20 kHz.

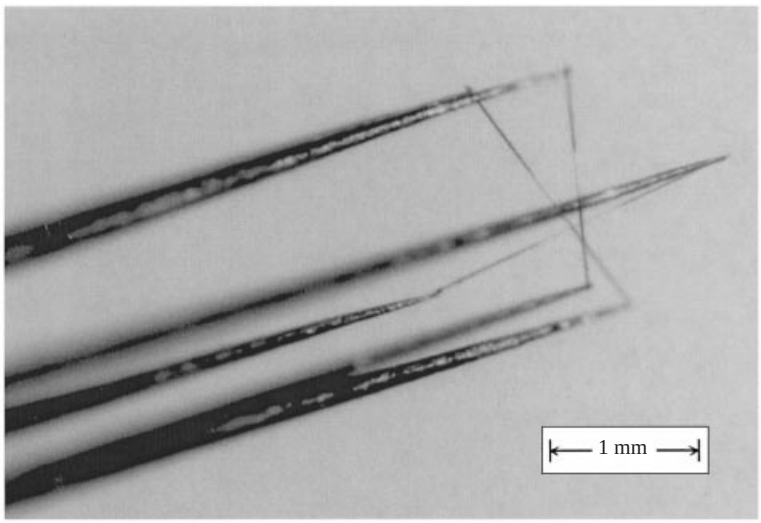

FIGURE 4. Photo of the triple hot-wire probe (THWP).

By applying a mixture of petroleum, oleic acid and laser-printer toner, a visual overall picture of the direction of the wall streamlines in the test section was obtained with an estimated error of $\pm 1^\circ$ (see also Schwarz & Bradshaw 1992).

The static pressure distribution in the test section was measured by means of the 1128 pressure taps (0.5 mm diameter) which were connected via a computer controlled 48 channel Scanivalve (model J, CTRL2 52–56 controller) to pressure transducers (Furness Controll or ELECTOR) with measuring ranges of 0.5, 1, 5 and 10 mbar. The output signal was converted to a RS232 signal using a DGH D 1000 series A/D converter with a sampling rate up to 7 Hz.

Skin-friction measurements were performed by a surface fence (e.g. Vagt & Fernholz 1973) and a wall hot-wire probe (WHWP) (e.g. Wagner 1991; Fernholz *et al.* 1996) both calibrated by means of a Preston tube (1.5 mm diameter) in the zero-pressure-gradient (ZPG) region (station $1M$ of figure 5). The two skin-friction probes were used to measure the magnitude and, by rotation, the direction of the skin friction vector while the WHWP provided also its fluctuating value. The wire of the WHWP was located 60 μm above the wall, had a diameter of 2.5 μm, an active sensor length of 0.5 mm, and gold-plated ends. The error estimate for the surface flow direction measured by the fence is $\pm 0.3^\circ$ with a repeatability of $\pm 0.1^\circ$. The value of mean skin friction from the WHWP deviates on average by $\pm 2\%$ from that of the surface fence with maximum deviations of up to 6% at the two stations furthest downstream ($10D$ and $11D$).

Instantaneous velocity vectors were measured in the boundary layer by means of a THWP and all components of the Reynolds stress tensor and the relevant triple correlations were determined. Details about this miniature probe and its calibration are given in Bruns & Dengel (1998). Figure 4 shows the THWP with wires arranged on the sides of an equilateral triangle when viewed from the front. The size of the measuring volume is defined by the height of this triangle $h = 0.39$ mm which is roughly equivalent to $h^+ = 16$ in wall units. All probes were built at the Hermann-Föttinger-Institut (HFI).

From the wall to $y^+ \approx 100$ the flow angle α and the velocity components U, W (note

Turbulence intensity	Corresponding wall distance	$\overline{u^2}$ SHWP	$\overline{v^2}$ and $\overline{w^2}$ THWP	$\overline{uv}$ and $\overline{uw}$ THWP	$\overline{vw}$ THWP
30%	$y^+ = 10$	−2.5%	—	—	—
20%	$y^+ = 30$	−1%	−6%	−10%	−15%

TABLE 1. Estimate of hot-wire uncertainties.

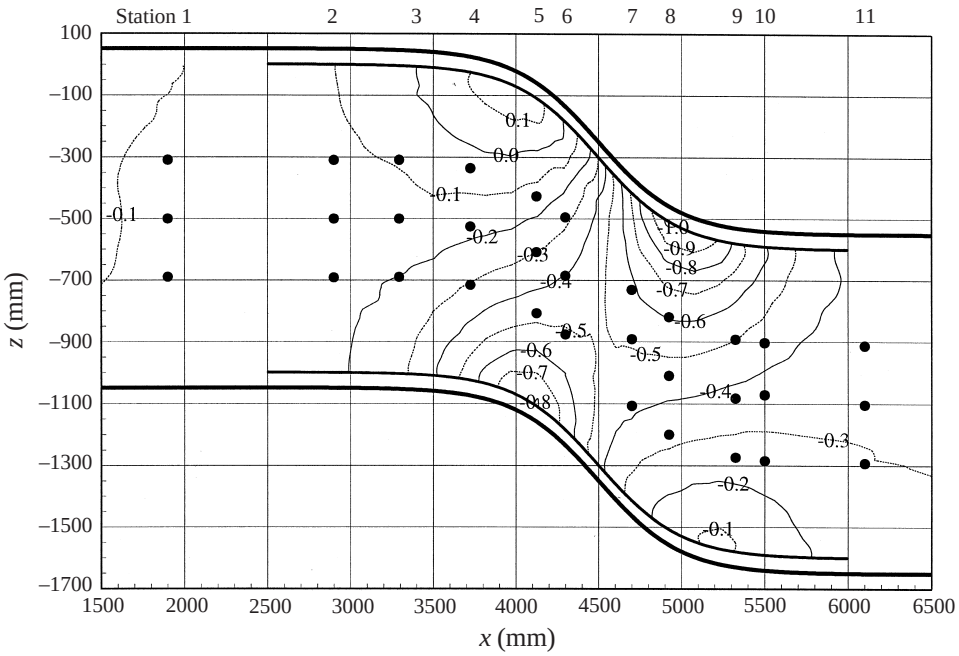

FIGURE 5. Iso-contours of the pressure coefficient c_p in the test section.

that mean velocities are denoted by capital letters without overbars throughout the text), u' and w' (the fluctuating components of the velocity) were measured by a single-wire probe (SHWP) with prongs that were traversed through its rotatable wall plug in order to cause a minimal flow disturbance. Both the THWP and the SHWP were equipped with 2.5 μm wires with gold-plated ends and an active length l to diameter d ratio of 200. The hot-wire probes were operated using constant-temperature hot-wire anemometers (TSI-IFA 100). Each hot-wire signal was amplified and filtered with a cut-off frequency of 20 kHz using a built-in signal conditioner. The data were recorded and stored on a transient recorder (Krenz TRC 6010) with three A/D channels of 12 bit resolution. For further processing the data were transferred to a Pentium PC via a GPIB interface. At each measuring point 32 ksamples were recorded at a sampling rate of 1 kHz with the filter cutoff reduced to 500 Hz. In order to achieve a higher frequency resolution, spectra and space correlations were measured with a sampling rate of 50 kHz.

During the development period of the THWP many comparative measurements were performed using X-wire probes (XHWP) for the $\overline{u'v'}$- and $\overline{u'w'}$-components. A detailed description may be found in Bruns (1998) and it suffices here to note that for locations $y^+ > 100$ the various miniature probes showed good agreement.

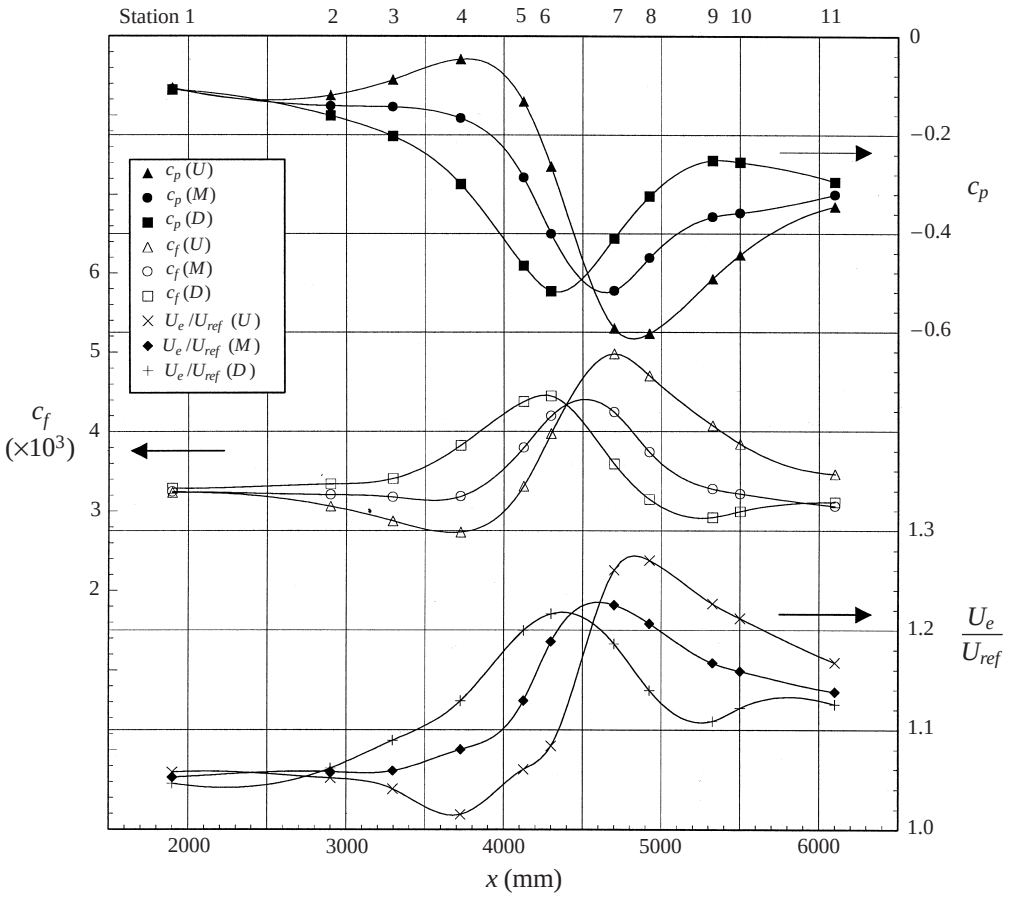

FIGURE 6. Pressure coefficient (top), skin-friction coefficient (middle) and magnitude of external velocity (bottom, with $U_{ref} \approx 16\ \mathrm{m\,s^{-1}}$) on the three lines ($U$), ($M$) and ($D$).

Uncertainties for the THWP are presented in table 1 for wall distances $y^+ = 10$ and 30% for the observed typical turbulence intensities of 30% and 20%, respectively.

3. Mean flow evolution

A first impression of the flow conditions on the test plate of the 'S'-duct is obtained from the iso-lines of the pressure coefficient c_p, cf. (3.1), on the test plate shown in figure 5, where the coordinates of the measuring stations for mean velocity and Reynolds stress profiles are shown again. The station numbers 1 to 11 used in the following refer to common x-positions (in tunnel coordinates) on the three lines (U = up), (M = middle) and (D =down) of figure 3.

Figure 6 shows the detailed development of the pressure coefficient c_p, the skin-friction coefficient c_f and the magnitude of the external or free-stream velocity U_e at the edge of the boundary layer along the three lines (U), (M) and (D). Here, c_p and c_f are defined as

$$c_p = \frac{p(x,z) - p_{ref}}{\frac{1}{2}\rho U_{ref}^2} \tag{3.1}$$

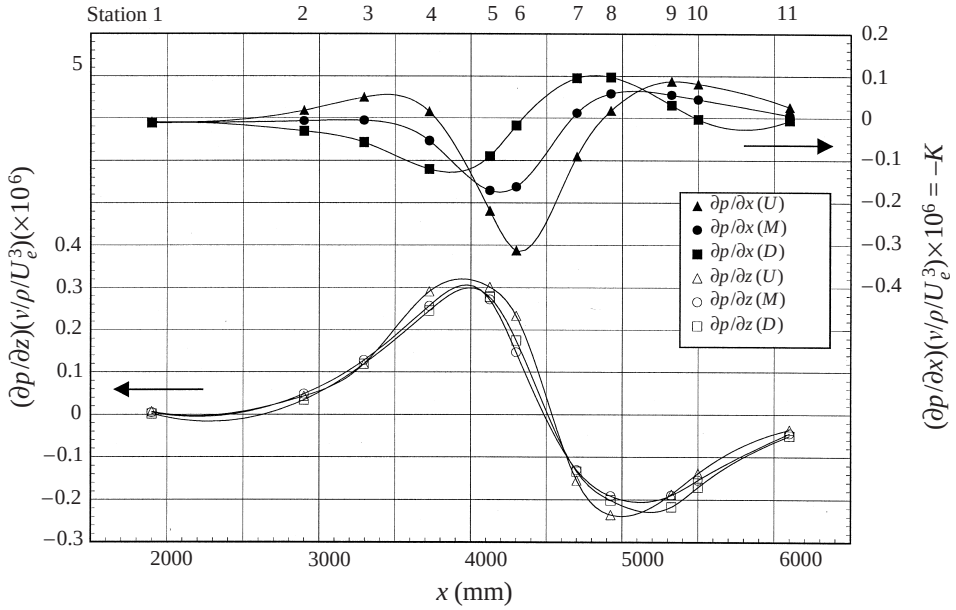

FIGURE 7. Distribution of the non-dimensionalized pressure gradients $\partial p/\partial x$ and $\partial p/\partial z$ in the external streamline coordinate system on lines (U), (M) and (D).

and

$$c_f = \frac{\overline{\tau}_w(x,z)}{\frac{1}{2}\rho U_{ref}^2}, \tag{3.2}$$

where $p(x,z)$ is the wall static pressure, $\overline{\tau}_w(x,z)$ the magnitude of the wall shear stress measured by the surface fence and U_{ref} the mean velocity at the entrance of the test section. The unit Reynolds number at the entrance of the test section was kept constant equal to $U_{ref}/\nu = 10^6\,\mathrm{m}^{-1}$, $U_{ref} \approx 16\,\mathrm{m\,s}^{-1}$ throughout this study.

The streamwise pressure gradients are both favourable and adverse, with the strongest variation along (U) and the weakest one along (M). The c_f-distributions are seen to be essentially mirror images of the c_p-distributions (cf. Fernholz & Warnack 1998). This reflects the dominant influence of the streamwise pressure gradient on the skin-friction coefficient.

The local pressure gradients $\partial p/\partial x$ and $\partial p/\partial z$ along and normal to the local external streamline, i.e. in the external streamwise coordinate system which will be used for most of the following presentation, are plotted in figure 7, made non-dimensional with $\rho U_e^3/\nu$ (the relation between the local external velocity U_e and and U_{ref} is given by figure 6). While the streamwise gradients show marked differences between the lines (U), (M) and (D), the history of the spanwise gradient is essentially the same on all three lines.

In order to relate the external streamline coordinate system of figure 2 and the wall streamline coordinate system to the tunnel coordinate system of figure 3, the development of the angle β of the freestream velocity vector $\boldsymbol{U}_e$ and that of the surface streamline α_w with respect to the tunnel coordinate system (TCS) are given in figure 8(a), while the maximum skewing angle $(\alpha_w - \beta)$ is plotted in figure 8(b). The heavy line in both graphs represents the angle of the tunnel sidewalls. Skewing of the mean velocity in the negative spanwise direction is seen to increase until station 5, then decrease and change sign between stations 8 and 9, where cross-over profiles are found along all three lines but most distinctly along line (D).

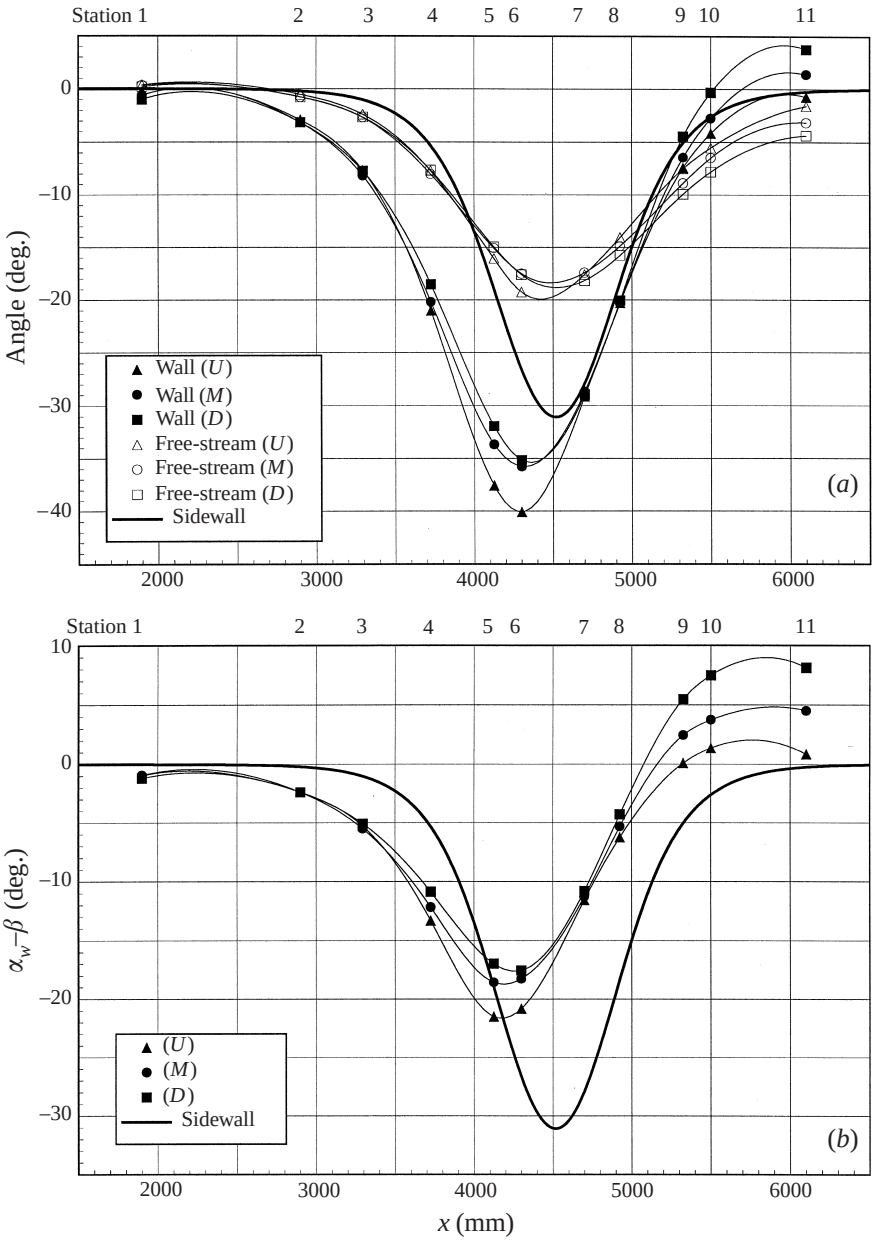

FIGURE 8. (*a*) Development of the mean flow angle in the free stream (β) and at the wall (α_w) relative to the tunnel coordinate system. (*b*) Maximum skewing angle ($\alpha_w - \beta$).

Based on the similarity of the development of c_p and c_f along the three lines (U), (M) and (D) on the test plate we restrict the following presentation of the effects of the streamwise and spanwise pressure gradients on the mean and fluctuating velocity profiles mainly to the stations 1–11 of line (U), while effects specifically associated with cross-over profiles will be discussed mostly on lines (M) and (D). A complete documentation for all measuring stations can be found in Bruns (1998).

The profiles of mean velocity magnitude $(U^2 + W^2)^{1/2}$ are plotted in figure 9 in

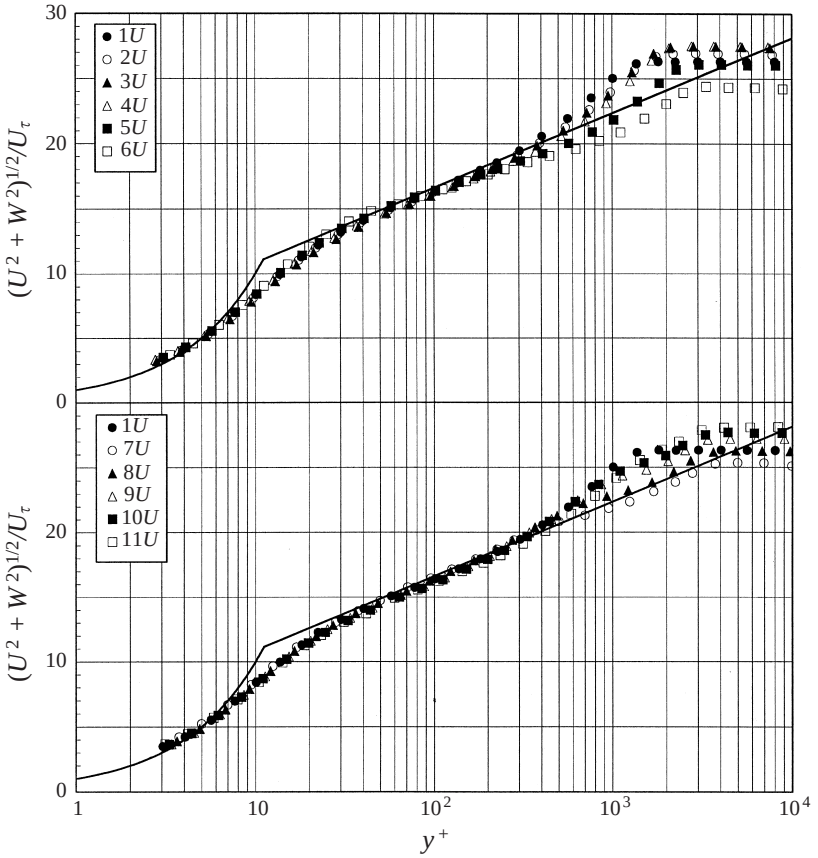

FIGURE 9. Profiles of the mean velocity magnitude $(U^2 + W^2)^{1/2}$ in inner-law scaling on line (U). The solid line indicates the linear and logarithmic law for a ZPG boundary layer.

inner-law scaling, i.e. made dimensionsless by $U_\tau = (\overline{\tau_w}/\rho)^{1/2}$ and ν/U_τ, with $\overline{\tau_w}$ the magnitude of the wall shear stress as measured by a surface fence and a wall hot-wire probe, methods independent of the logarithmic law of the wall.

In the inner region of the boundary layer (linear and logarithmic region) the mean velocity *magnitude* essentially follows the profile for two-dimensional boundary layers with zero pressure gradient shown as solid line on figure 9 (for the log-law, the Kármán constant $\kappa = 0.40$ and the intercept $c = 5.10$ was used), and this independently of the mild streamwise and spanwise pressure gradients. It is somewhat surprising that the log-law and the linear law in the viscous sublayer still hold even for cross-over profiles, suggesting that for our conditions the u-momentum is largely dominant over the w-momentum. Deviations from the logarithmic law are to be expected only for more strongly accelerated velocity profiles (e.g. Fernholz & Warnack 1998). For an extensive review of the near-wall similarity laws the reader is referred to Ölçmen & Simpson (1992).

In the wake region, deviations are already expected at values of the acceleration parameter $K = (\nu/U_e^2)(\partial U_e/\partial x)$ of the order of 0.3×10^{-6} and are indeed observed in the present 3DTBL for the same K-range (station $6U$ of figure 7). For the less accelerated profiles Coles' wake function $\Delta U/U_\tau$, ranging between approximately 3 in the ZPG-region and -1 at the end of the acceleration along line (U), is lower

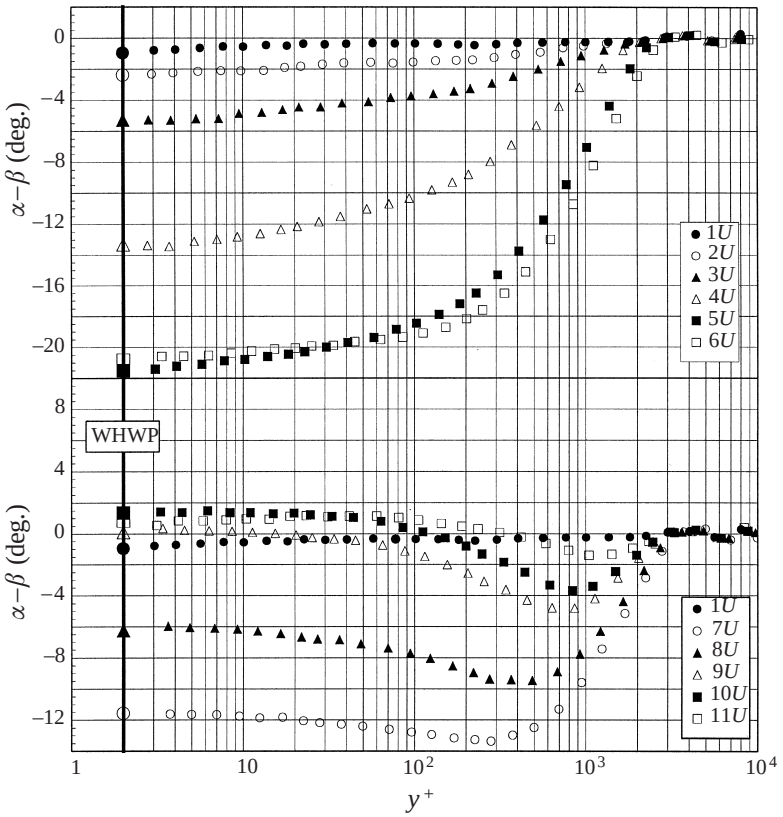

FIGURE 10. Profiles of the local flow angle $(\alpha - \beta)$ relative to the free-stream direction on line (U).

than expected. It must therefore be assumed that the increase of $(U^2 + W^2)^{1/2}$ is balanced by an equivalent increase of U_τ. This is indeed the case because c_f-values calculated for a two dimensional flow are smaller than those measured in the present three-dimensional boundary layer (see Bruns 1998, his figure 4.6).

The profiles of the skew angle $\alpha(y^+) - \beta$, corresponding to the profiles of figure 9 were determined from single hot-wire measurements with the rotation technique, while the wall flow angles were measured with the wall hot-wire probe located at $y^+ \approx 2$. They are presented in figure 10 which shows a monotonic decrease of the skew angle towards the wall up to station $6U$ with an overall minimum of $-22°$. Beyond station $7U$ the skew angle minimum moves away from the wall and the wall skew angle increases again, crosses zero and reaches a maximum of $+2°$ at station $10U$. As mentioned before, this cross-over effect is larger along line (D) where the wall skew angle ranges from $-18°$ to $+8°$ (not shown here).

To compare the cross-flow behaviour in the outer region with the semi-empirical model proposed by Squire & Winter (1951) and Hawthorne (1951), the Squire–Winter–Hawthorne (S-W-H) relation

$$\frac{W}{U_e} = 2\beta \left(1 - \frac{U}{U_e}\right), \tag{3.3}$$

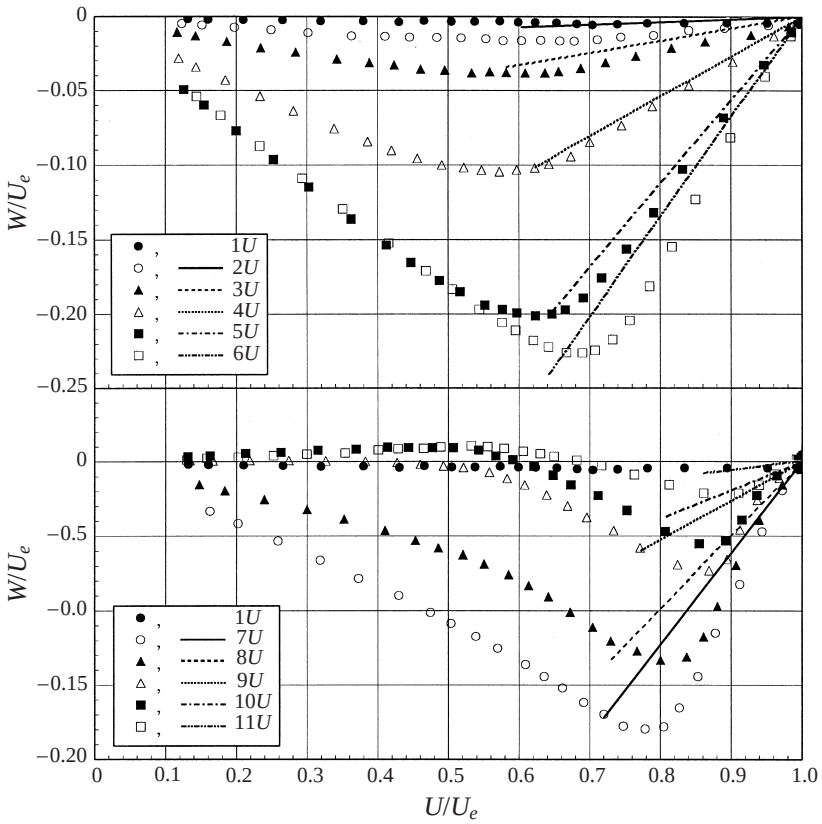

FIGURE 11. Polar plot of mean velocity components and the S-W-H relation along line (U)

the velocity components U and W in the external streamline coordinate system are presented as polar plots (Gruschwitz 1935; Johnston 1960). Figure 11 pertains to line (U) on which the strongest crossflow velocity W reaches 23% of U and figure 12 displays the strong cross-over profiles along line (D).

It is obvious from the comparison of our data with the S-W-H relation in figures 11 and 12 that the latter is only useful for mild cross-flow (see also Schwarz & Bradshaw 1993) and fails when cross-over profiles occur.

The present data also allow the resolution of a long lasting discussion in the literature on whether the direction of the velocity close to the wall is constant or not in a 3DTBL (a recent example is Parneix & Durbin 1997). If this were the case, an isotropic eddy viscosity assumption could be used for closure, at least in the wall region. There is numerical evidence by Pierce & East (1972) and Klinksiek & Pierce (1973) that the direction of the velocity is not constant as the wall is approached whereas Goldberg & Reshotko (1984) conclude from a theoretical analysis, based on matched asymptotic expansions, that velocity vectors are coplanar† near the wall. It appears, however, that this latter analysis is not applicable for $y \to 0$. Instead, we develop all velocity components in Taylor series around $y = 0$ and obtain in a

† We think that 'coplanar' is more appropriate than the term 'collateral' used in the literature.

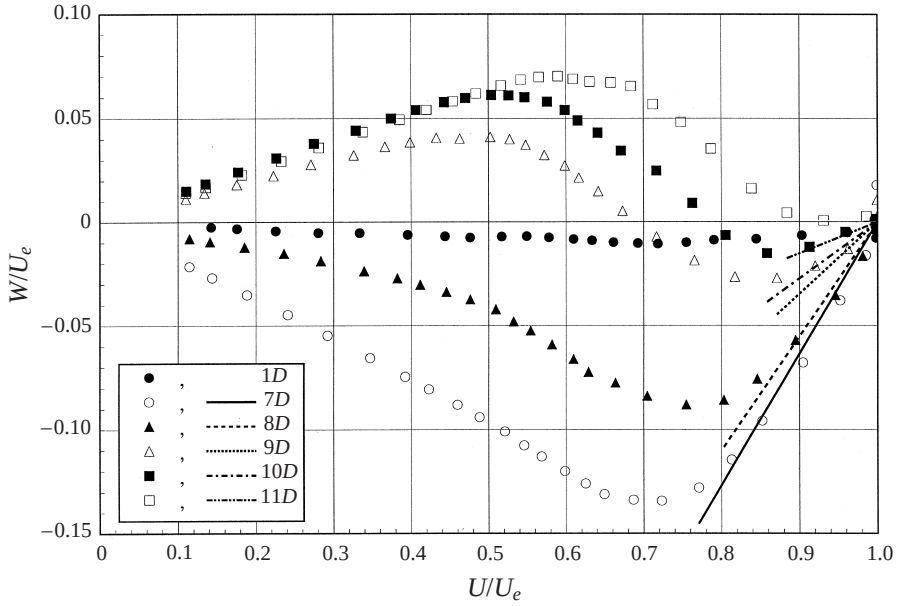

FIGURE 12. Polar plot of the mean velocity components and the S-W-H relation along the downstream part of line (*D*).

straightforward manner the result for $(\alpha - \alpha_w) \to 0$

$$\alpha - \alpha_w \approx \frac{W}{U} = \tfrac{1}{2}\Pi_z^{(WSCS)} y^+ (1 - \tfrac{1}{2}\Pi_x^{(WSCS)} y^+) + 0(y^{+3}) \tag{3.4}$$

where $\Pi_x^{(WSCS)} = (\nu/\rho U_\tau^3)\partial p/\partial x$ and $\Pi_z^{(WSCS)} = (\nu/\rho U_\tau^3)\partial p/\partial z$ are the streamwise and cross-stream pressure gradients in wall-streamline coordinates. Since Reynolds stresses enter the solution only at $O(y^{+3})$, the above relation is exact to $O(y^{+2})$ and shows that for $\Pi_z^{(WSCS)} \neq 0$ *no region of coplanar velocity vectors* exists next to the wall.

The evaluation of the above relation for the flow angle requires accurate measurements of the pressure gradients as well as of the skin-friction velocity. Direct measurements of the near-wall flow angle by means of hot-wire or three-hole probes are often detrimentally affected by probe/flow interference (e.g. Vagt & Fernholz 1979). However, the WHWP and the SHWP traversed through the wall (as in Rogers & Head 1969) have provided sufficiently accurate data which are compared with (3.4) on figure 13 where the flow angle is plotted linearly against y^+.

Up to station $6M$ and for stations $10M$ and $11M$ the wall slope of the skew angle $(\alpha - \beta)$ agrees well with the theory, if one makes allowances for an occasional inconsistency of up to 0.5° between the WHWP at $y^+ \approx 2$ and the SHWP. In the cross-over region however, at stations $7M$–$9M$, the sign of the slope at the wall already does not agree. This inconsistency may be due to the hot-wire directionality being affected by a systematic error very near the wall, or the skew angle profile reaches the predicted wall slope only for $y^+ < 2$. Despite these shortcomings, our hot-wire data provide clear evidence against coplanar velocity vectors near the wall. Together with the evidence of Ölçmen & Simpson (1995*b*) who did not find a coplanar region down to $y^+ = 4$ using an LDA, this question should be definitively settled.

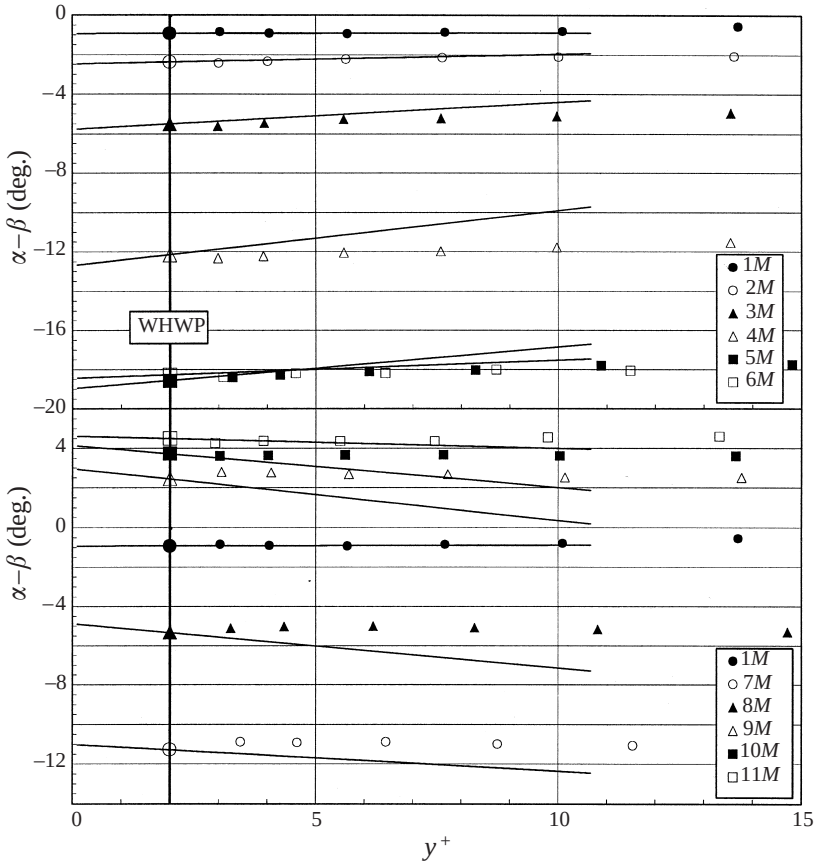

FIGURE 13. Comparison of the calculated with the measured flow direction near the wall on line (*M*).

4. Turbulence measurements

4.1. *Wall shear stress fluctuations*

To complement the mean skin-friction measurements of figure 6 the statistics of the fluctuating part of the skin friction τ_w', as measured by the WHWP at the dimensionless height of $y^+ = 1.8$, are documented in figure 14. The turbulence level is defined as $T_{\tau_w} = (\overline{\tau_w'^2})^{1/2}/\overline{\tau}_w$ and the skewness and flatness as $S_{\tau_w} = \overline{\tau_w'^3}/(\overline{\tau_w'^2})^{3/2}$ and $F_{\tau_w} = (\overline{\tau_w'^4})/(\overline{\tau_w'^2})^2$, respectively.

The general evolution of the three moments is qualitatively similar and rather as expected. For two-dimensional ZPG boundary layers in the Reynolds number range of this experiment typical values for S_{τ_w} and F_{τ_w} are 1 and about 4.5 (see e.g. Fernholz & Finley 1996) and maxima and minima here differ at most by +7% and −15% for both S_{τ_w} and F_{τ_w}. The location of the maxima and minima of T_{τ_w} lead those of S_{τ_w} and F_{τ_w} and correspond more or less with the extrema of the streamwise pressure gradient (cf. figure 7), whereas the extrema of S_{τ_w} and F_{τ_w} are both approximately at the same position as those of c_p itself (cf. figure 6). This reinforces the conclusion that the evolution of the skin friction is dominated by the streamwise pressure gradient.

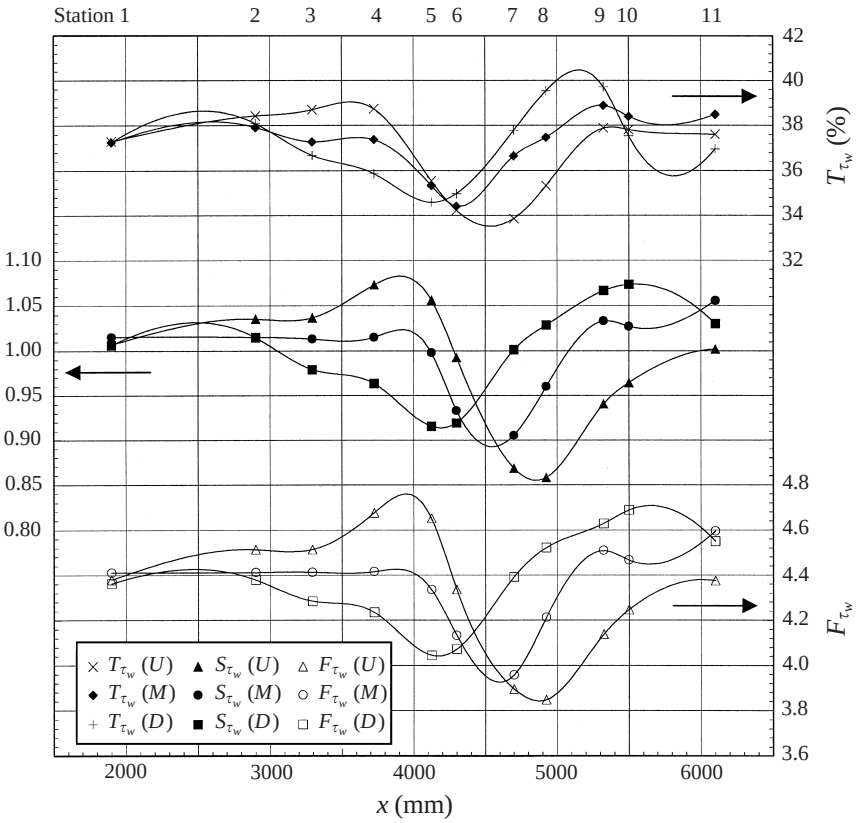

FIGURE 14. Turbulence level T_{τ_w}, skewness S_{τ_w} and flatness F_{τ_w} along the lines (U), (M) and (D).

4.2. *Reynolds stresses*

Profiles of the Reynolds stresses in inner-law scaling, i.e. plotted versus $y^+ = y(U_\tau/\nu)$, are collected in figures 15–24. All the stress components are defined with respect to the local external streamline coordinate system, since the discussion of the influence of different degrees of three-dimensionality and of the interaction between Reynolds stresses and mean flow is easiest in these coordinates. We recall that the measurements were carried out with the THWP for $y^+ \gtrsim 30$ and with the SHWP with prongs traversed through the wall for $y^+ \gtrsim 3$.

First, profiles are discussed in the region where skewing occurs in one direction only, approximately from stations $2U$ to $6U$, and where the streamwise pressure gradient is mostly favourable. Then profiles are presented in the cross-over and the initial part of the region where the adverse streamwise-pressure gradient falls to zero (cf. figure 7) and relaxation to two-dimensional flow occurs. It should be noted, however, that the streamwise pressure gradients in the present experiment are not severe compared with a highly accelerated (e.g. Fernholz & Warnack 1998) or a separating boundary layer (e.g. Dengel & Fernholz 1990).

In inner-law scaling the Reynolds normal stress $\overline{u'^2}/U_\tau^2$ shows a behaviour in the viscous sub-layer and the buffer layer up to its peak which is located between $14 \geqslant y^+ \geqslant 18$ (figure 15) which is similar at all stations as well as similar to the ZPG case (station $1U$ and Fernholz & Finley 1996, for instance). However, the

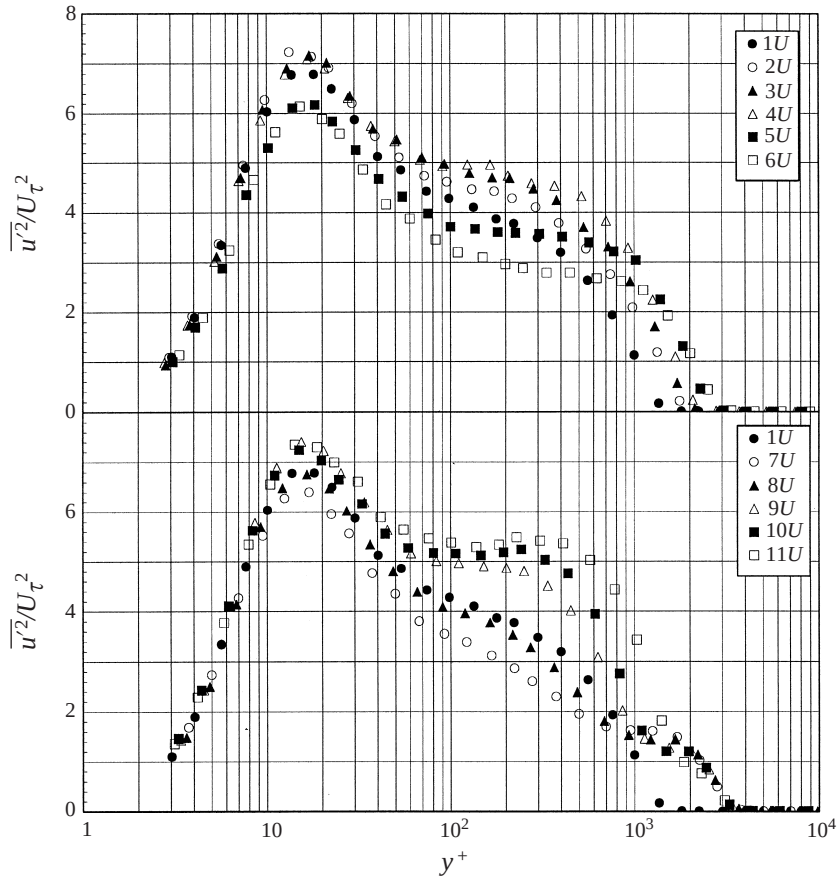

FIGURE 15. Profiles of the Reynolds normal stress component $\overline{\rho}\,\overline{u'^2}$ (ESCS) in inner-law scaling along line (U).

peak value decreases in the streamwise direction by about 15% to $(\overline{u'^2}/U_\tau^2)_{\max} = 6.1$ before it recovers to the initial value of about 7. Since the skin-friction velocity U_τ varies between 0.57 and 0.78 m s^{-1} in this x-range, most of the decrease can be attributed to the normalization by U_τ^2 and hence the effect of streamwise and spanwise pressure gradient remains small in the inner layer. The changes in the outer layer on the other hand are much stronger. Here the normal stress component $\overline{u'^2}/U_\tau^2$ responds strongly to the streamwise pressure gradient, increasing where it is adverse and decreasing where it is favourable. Noteworthy is the distinct plateau of increased stress with a small secondary peak at stations $9U$–$11U$ of figure 15 which is due to the adverse pressure gradient and possibly to the history accumulated in the cross-over region. Such 'plateau-type' profiles do occur in mild adverse-pressure-gradient two dimensional boundary layers (e.g. Dengel, Fernholz & Vagt 1981) because both the mean shear gradient $\partial U/\partial y$ and $\overline{u'v'}$ increase away from the wall thus augmenting the turbulence production further away from the wall (Alving & Fernholz 1996). The persistence of the plateau in a region where $\partial p/\partial x$ has become zero (downstream of station 9) suggests that crossflow or history accumulated in the cross-over region must be dominating the delayed relaxation to ZPG conditions. In particular, one might speculate about the role of the inflection point in the W-profile (see e.g. figure 11) which may promote local instabilities.

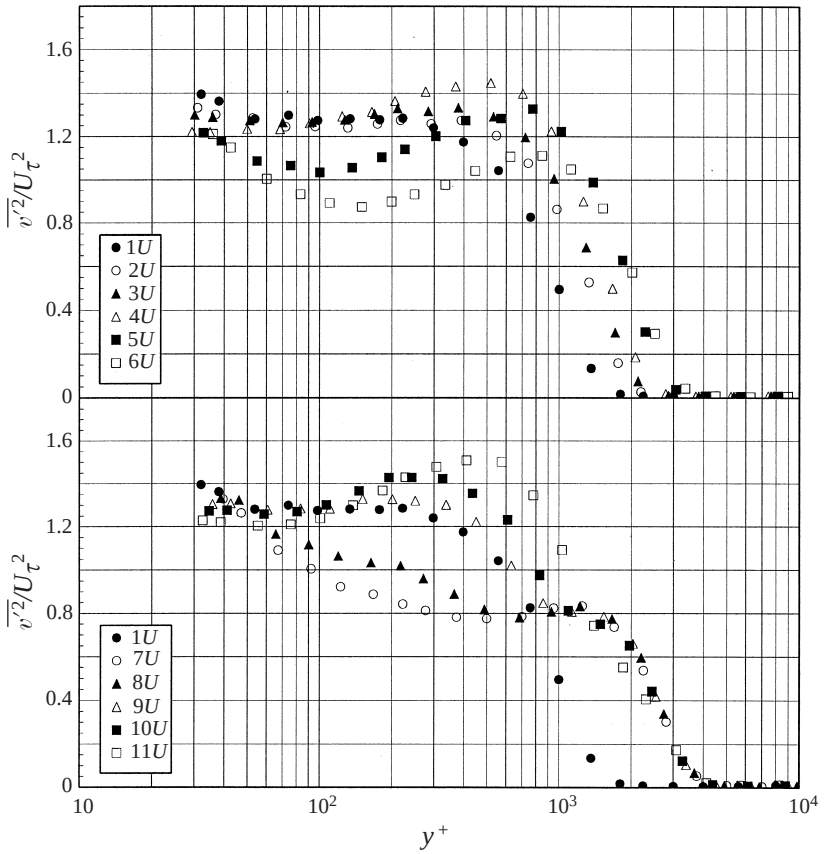

FIGURE 16. Profiles of the Reynolds normal-stress component $\overline{\rho}\,\overline{v'^2}$ (ESCS) in inner-law scaling along line (U).

Figure 16 presents the Reynolds normal-stress component $\overline{\rho}\,\overline{v'^2}$ in inner-law scaling. The profiles show two regions where distinct changes occur: a relative minimum around $y^+ \approx 150$ (station $6U$) and a plateau (stations $9U$ and $10U$) in the outer region at $y^+ \approx 1500$, followed by an overshoot over the initial ZPG profile ($1U$). The decrease of $\overline{v'^2}/U_\tau^2$ in the near-wall region is comparable with that found in a mildly accelerated two-dimensional boundary layer (Warnack 1996, data evaluated by the second author) and is due to a decrease of $\overline{\rho}\,\overline{v'^2}$ production, a process which then extends to the outer region of the boundary layer (stations $9U$ and $10U$) before $\overline{\rho}\,\overline{v'^2}$ increases again towards the exit of the 'S'-duct. This increase is much stronger than would normally be caused by the mild adverse pressure gradient (see also data along line (D) in Bruns 1998, his figure 5.9) and must therefore be attributed to the three-dimensionality of the flow or again to history effects. The slight increase of $\overline{v'^2}/U_\tau^2$ in the range below $y^+ \approx 80$ on the other hand is probably due to probe effects close to the wall (see Österlund & Johansson 1995). The magnitude of the peak value $(\overline{v'^2}/U_\tau^2)_{\max} \approx 1.30$ and the location of the peak at about $y^+ = 200$ for the ($1U$)-profile agree with the data of Fernholz & Finley (1996).

The third Reynolds normal stress profiles $\overline{w'^2}/U_\tau^2$ are presented in figure 17. Because of the production term $\overline{v'w'}\partial W/\partial y$ in the Reynolds stress transport equation for $\overline{w'^2}$ one would expect a higher level of $\overline{\rho}\,\overline{w'^2}$ in three-dimensional than in two-dimensional

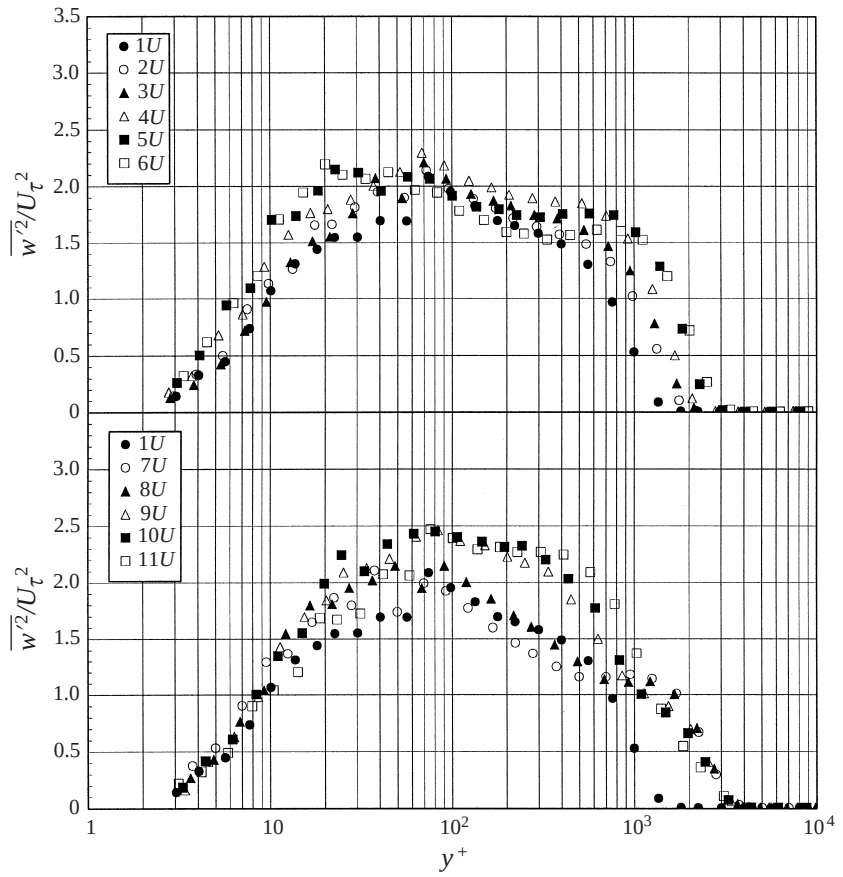

FIGURE 17. Profiles of the Reynolds normal-stress component $\overline{\rho}\,\overline{w'^2}$ (ESCS) in inner-law scaling along line (U).

boundary layers. This is in fact the case and the decrease of the stress level caused by the favourable pressure gradient in two-dimensional boundary layers (see Warnack 1996) is compensated leading to values above the initial ZPG profile. The latter is in agreement, both in magnitude and location of the peak, with measurements of Warnack. In the cross-over region the spanwise normal stress levels in the log-range are about 40% higher than in the initial ZPG profile and show self-similar behaviour in the viscous sublayer and in the buffer layer. The largest deviations from the initial ZPG profile at stations 1 occur in the downstream part of the 'S'-duct along line (D) where the cross-over effect is strongest and are shown in figure 18.

The profiles of twice the turbulent kinetic energy (the sum of all the normal Reynolds stresses $\overline{q'^2}$) along line (U) follow those of $\overline{\rho}\,\overline{u'^2}$, which is its main contributor, but develop a more distinct plateau starting further upstream (figure 19). The maximum level of the plateau ($\overline{q'^2}/U_\tau^2 \approx 9$) on line ($U$) increases in the region of strongest cross-flow on line (D) to even higher values of about 10 (not shown).

Of the three Reynolds shear stresses two, $\overline{\rho}\,\overline{u'w'}$ and $\overline{\rho}\,\overline{v'w'}$, exist only in three-dimensional boundary layers. So streamwise pressure-gradient effects should be more evident in the $\overline{\rho}\,\overline{u'v'}$-profiles while cross-flow effects should dominate the two other components via, for example, the production terms containing the gradient

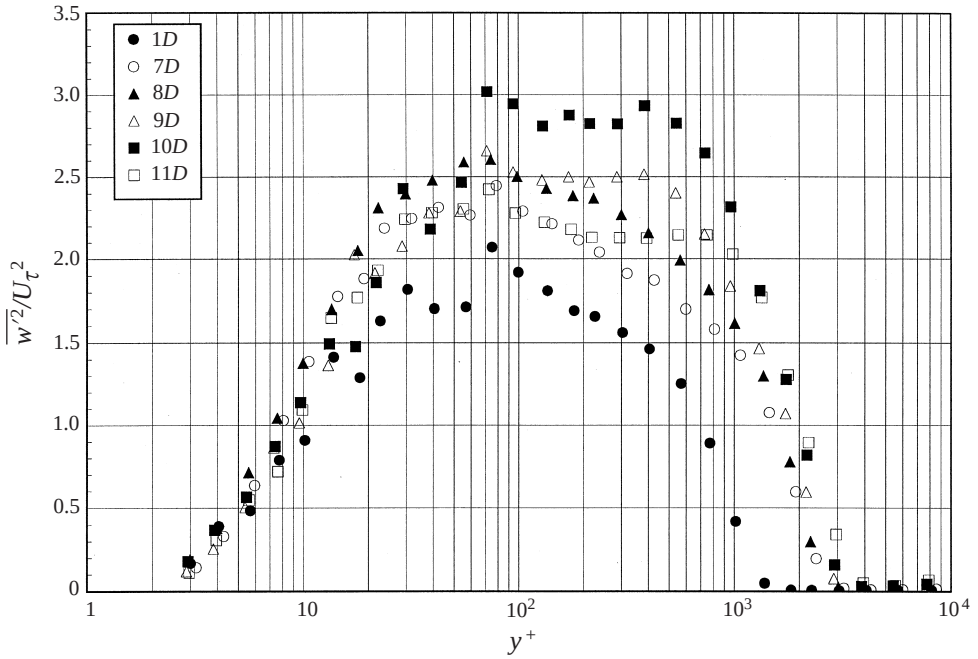

FIGURE 18. Profiles of the Reynolds normal-stress component $\overline{\rho}\,\overline{w'^2}$ (ESCS) in inner-law scaling along line (D) in the cross-over region.

$\partial W/\partial y$. Therefore, to facilitate the following discussion, the profiles of this mean velocity gradient along the line (U) are presented first in figure 20.

The $\overline{\rho}\,\overline{u'v'}$-profiles along line ($U$) are shown in figure 21. We note at this point that the maximum value of the $\overline{u'v'}$-profile at station $1U$ is about 12% below the value found in a canonical two dimensional boundary layer (e.g. Fernholz & Finley 1996). It has been verified that this is a peculiarity of the Lausanne wind tunnel, possibly a remnant of the tripping, and not a probe effect. The magnitude of $\overline{u'v'}$ clearly decreases with increasing streamwise acceleration up to station $7U$ and then increases again in the adverse-pressure-gradient and cross-over region (stations $8U$ to $11U$) with an overshoot over the initial ZPG profile in the outer layer. The decrease in magnitude of $\overline{\rho}\,\overline{u'v'}$ is consistent with the decrease in $\overline{\rho}\,\overline{v'^2}$ appearing in the main production term $\overline{v'^2}\,(\partial U/\partial y)$ as well as with the numerical results of Sendstad & Moin (1992). The behaviour of the Reynolds shear stress is however opposite to that described by Schwarz & Bradshaw (1993), who found an increase of $|\,\overline{\rho}\,\overline{u'v'}\,|$ as skewing increased. This may be due to the zero streamwise pressure gradient in the Schwarz & Bradshaw boundary layer but we do not find this explanation satisfactory since in our measurements cross-flow effects do not appear to increase $|\,\overline{u'v'}\,|$ and a zero streamwise pressure gradient does not lead to an increase either. The remaining possible culprits are measurement error and history effects.

Figure 22 shows that the $\overline{\rho}\,\overline{v'w'}$ component of the Reynolds shear stress which, added vectorially to $\overline{\rho}\,\overline{u'v'}$ yields τ_{tot}, increases in the streamwise direction with cross-flow. The profiles develop two extrema with the larger one reaching $(\overline{v'w'}/U_\tau^2)_{\max} = -0.3$ at the upper end of the log-region $y^+ \approx 800$ of station $5U$, which is roughly one third of that of $\overline{\rho}\,\overline{u'v'}$. The relevant production term for $\overline{v'w'}$ is $\overline{v'^2}\partial W/\partial y$ and, since $\overline{v'^2}$ does not change much in this region (cf. figure 16), it is the gradient $\partial W/\partial y$ and its sign

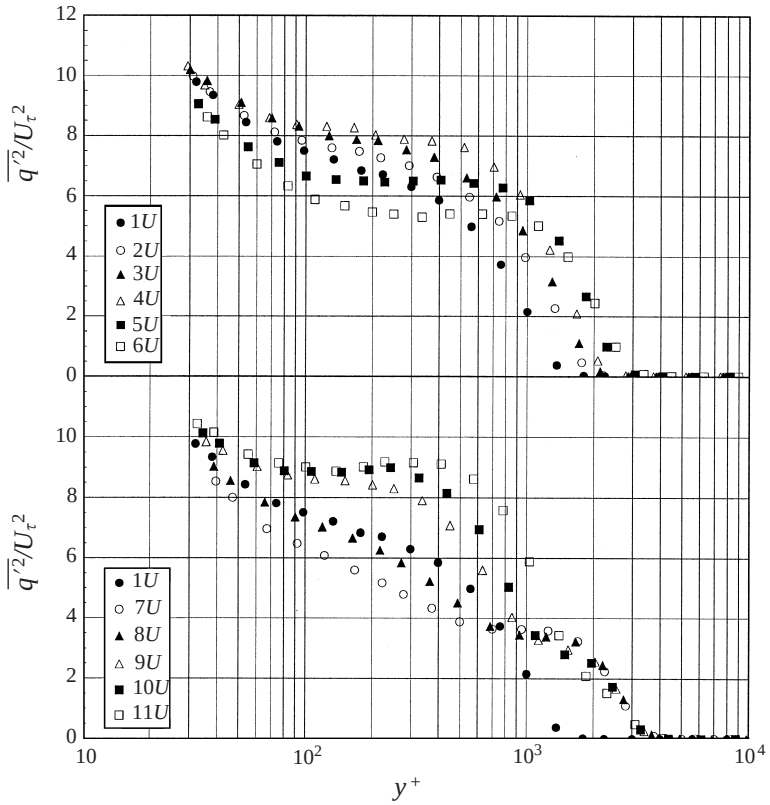

FIGURE 19. Profiles of twice the kinetic turbulent energy in inner-law scaling along line (U).

which determines the shape of the $\overline{\rho}\,\overline{v'w'}$-profile. A comparison of figures 20 and 22 shows that the maxima and minima of $\partial W/\partial y$ indeed line up approximately with the minima and maxima, respectively, of $\overline{\rho}\,\overline{v'w'}$. It is also noted that the sign change of the shear stress occurs further out in the boundary layer with increasing streamwise distance x.

Since the third Reynolds shear stress component, $\overline{\rho}\,\overline{u'w'}$, does not appear in the three-dimensional boundary layer equations, its discussion is often omitted. As shown in figure 23, it reaches however peak values twice as large as $\overline{\rho}\,\overline{u'v'}$ in the upstream bend of the 'S' (stations $5U$ and $6U$) which is in general agreement with the results of Ölçmen & Simpson (1995*b*). From station 1 to 6, the sign of $\overline{\rho}\,\overline{u'w'}$ is negative near the wall with a minimum at $y^+ \approx 15$ which agrees with the DNS of Sendstad & Moin (1992). The profiles then cross zero at $y^+ \approx 150$, reaching a smaller maximum at $y^+ \approx 1000$. In this region the behaviour of $\overline{\rho}\,\overline{u'w'}$ is almost identical along the three lines (we show only profiles along line U) indicating that the spanwise pressure gradient is dominant while the influence of the streamwise pressure gradient is minimal.

Downstream of station 6, the character of the profiles on line (U) changes and the profiles along the lines (U) and (D) start to differ significantly (figures 23 and 24) because of the different cross-over profiles. This behaviour can be explained by the change of sign of the spanwise pressure gradient and by the evolution of the two main production terms, $\overline{v'w'}\partial U/\partial y + \overline{u'v'}\partial W/\partial y$ in the Reynolds transport equation for $\overline{u'w'}$. Since $\overline{u'v'}$ is always negative, the second production term changes sign with

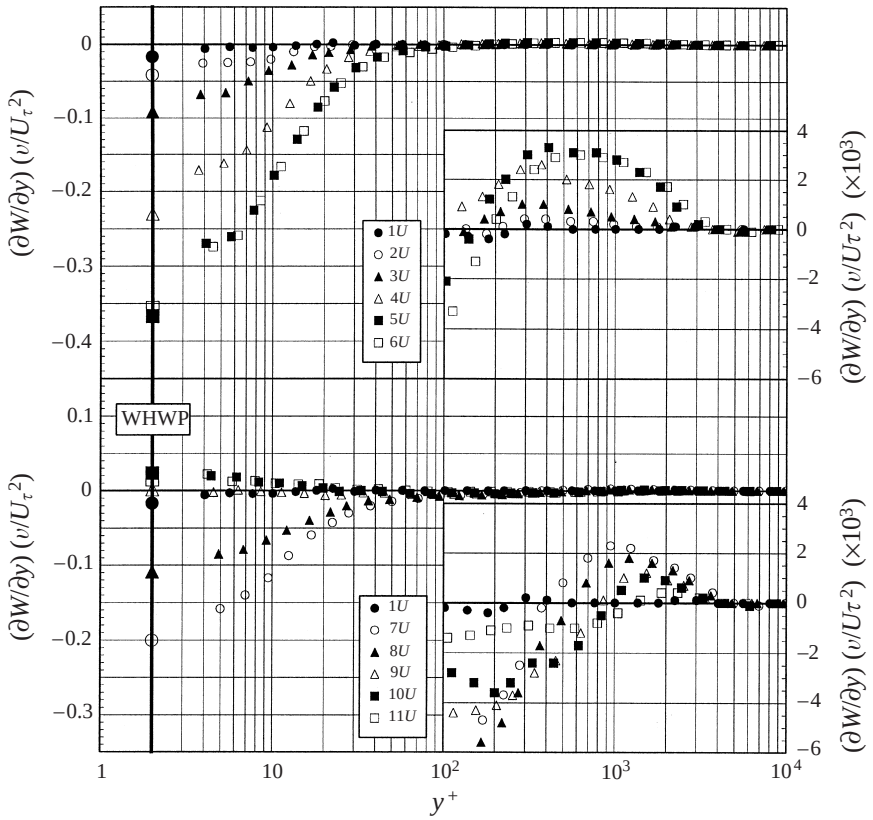

FIGURE 20. Profiles of the mean spanwise velocity gradient (ESCS) in inner-law scaling along line (U).

$\partial W/\partial y$ from positive near the wall to negative further out in the boundary layer and, with $\partial U/\partial y$ always positive, the first production term changes sign with $\overline{v'w'}$ from positive near the wall to negative further out. This also explains the relatively large negative value of $\overline{\rho}\,\overline{u'w'}$ close to the wall because both production terms have the same sign.

The change of sign of the spanwise pressure gradient has the effect that on line (U) near the wall $\overline{\rho}\,\overline{u'w'} \to 0$ for increasing downstream distance. Further out in the profile, the region of $\overline{\rho}\,\overline{u'w'} > 0$ virtually disappears and a new small negative peak develops which then starts to decay at the last station where the boundary layer is relaxing to two dimensional conditions. It is interesting to note that the y^+-location where $\overline{u'w'}$ changes sign corresponds closely to the largest zero-crossing of $\partial W/\partial y$ (compare figure 23 with the enlarged inserts in figure 20 and see Bruns 1998). These effects are much more pronounced along line (D) where the two extrema of the upstream profiles (e.g. at $6U$ of figure 23) are essentially flipped over at stations $9D$ to $11D$ of figure 24.

4.3. *Characteristic flow angles*

An idea about the link between the behaviour of mean flow and turbulent fluctuations in a three-dimensional boundary layer can be gained from the profiles of the skew angle of the mean velocity ($\alpha - \beta$), the mean shear angle γ_g and the Reynolds shear

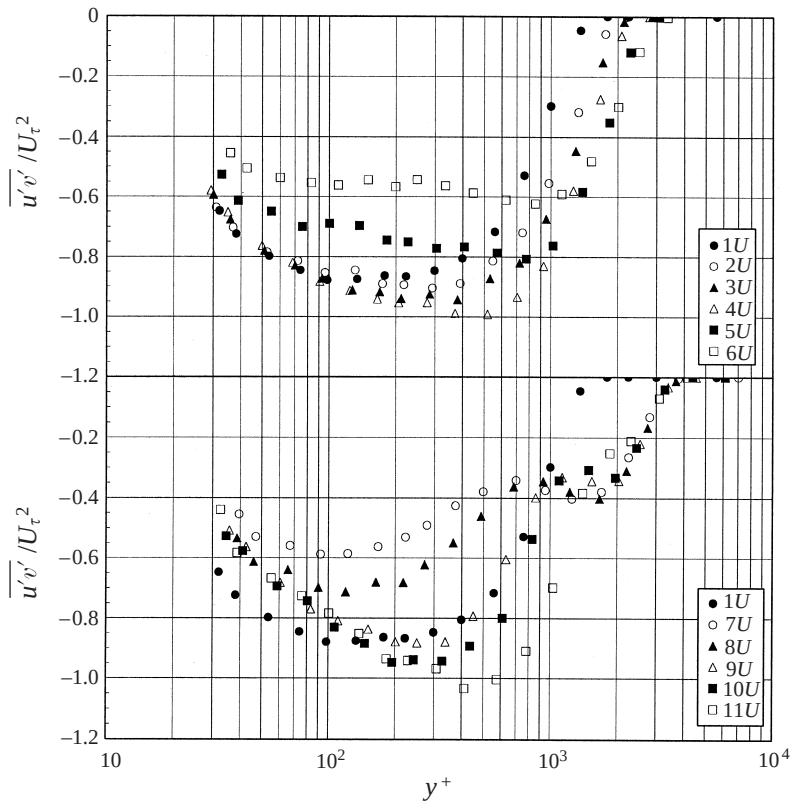

FIGURE 21. Profiles of the Reynolds shear stress $\overline{\rho}\,\overline{u'v'}$ (ESCS) in inner-law scaling along line (U).

stress angle γ_τ. The last two are defined by

$$\gamma_g = \tan^{-1}\left(\frac{\partial W/\partial y}{\partial U/\partial y}\right) \quad \text{and} \quad \gamma_\tau = \tan^{-1}\left(\frac{\overline{v'w'}}{\overline{u'v'}}\right). \tag{4.1}$$

In most but not in all pressure-driven boundary layers with unilateral skewing γ_τ lags behind γ_g indicating that the turbulence structure needs time to adapt to the changes in the mean shear field. It is also to be expected that the size of the lag will vary between the wall and the edge of the boundary layer, decreasing when the wall is approached.

Figure 25 shows profiles of the three angles $(\alpha - \beta)$, γ_g and γ_τ in inner-law scaling at three stations on the lines (U) and (D), respectively. The first two stations, 4 and 6, are in the range of the upstream bend and the shear stress vector lags the velocity gradient vector over a larger y^+-interval at station 4 than at station 6 where the turbulence had more time to adjust to the mean shear. All three profiles collapse onto one line in the near-wall region. This is also more or less the case for the measurements of Compton & Eaton (1995) but not for those of Ölçmen & Simpson (1996) where γ_τ lags γ_g. The profiles at stations $10U$ and $10D$ are characteristic of cross-over behaviour and all three angles change sign twice. The disappearance of the the lag between γ_τ and γ_g is due to the change of sign of the spanwise pressure gradient and the reduction of γ_g, while relaxation is not thought to play a role.

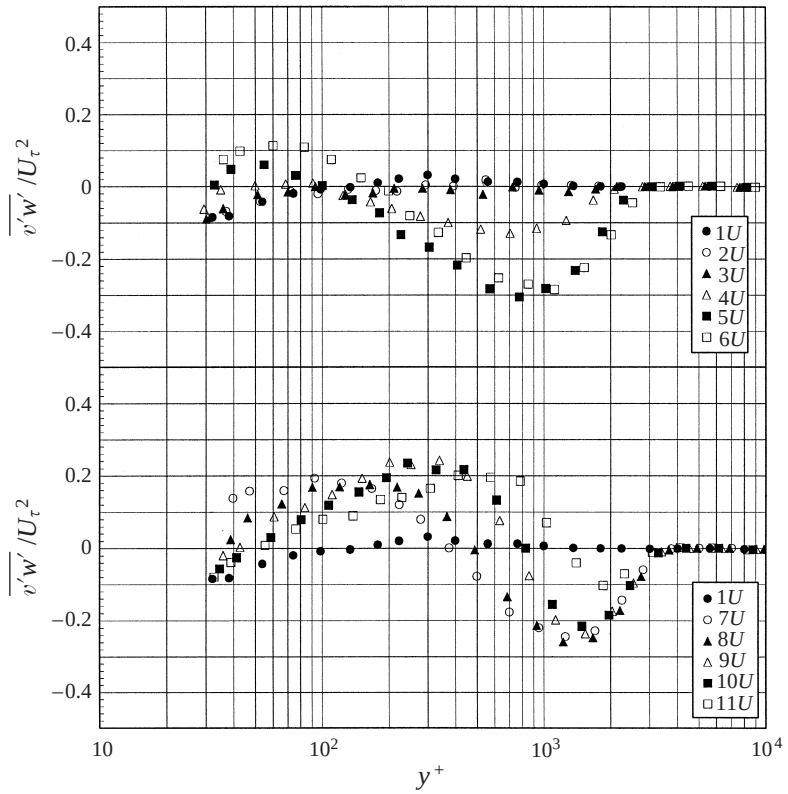

FIGURE 22. Profiles of the Reynolds shear-stress $\overline{\rho}\,\overline{v'w'}$ (ESCS) in inner-law scaling along line (U).

4.4. *Triple correlations*

Triple products of the fluctuating velocities must be known for the evaluation of the turbulent diffusion terms in the Reynolds-stress transport equations. The whole set of triple-correlation profiles was measured and presented in Bruns (1998). Here we confine the discussion to the $\overline{u'v'^2}$- and $\overline{v'^2w'}$-profiles which are important for the transport of $-\overline{u'v'}$ and $-\overline{v'w'}$ and can be compared with the data of Schwarz & Bradshaw (1994) for $y/\delta > 0.15$ in the upstream bend of the 'S'-duct.

Data of $\overline{u'v'^2}/U_\tau^3$ in a two-dimensional ZPG boundary layer for the same Reynolds number range as ours can be found in the literature, for instance in Erm (1988) and Fernholz & Finley (1996, their figure 74). Their profiles agree qualitatively with the present profiles of $\overline{u'v'^2}$, shown in figures 26 and 27: they show a double minimum (the inner minimum on these figures is at $y^+ < 30$ and could not be reached by the THWP) and they scale on U_τ^3, revealing approximate self-similarity in the range $30 < y^+ < 100$ for the unilaterally skewed velocity profiles of stations 1–6 (cf. figures 26 and 27). This behaviour is in agreement with data of Warnack (1996) in a mildly accelerated two-dimensional layer, but disagrees with the measurements of Murliss, Tsai & Bradshaw (1982). In figures 26 and 27, as well as in Warnack (1996) the value of $\overline{u'v'^2}/U_\tau^3$ at the outer minimum is about -0.35 for ZPG conditions and varies between -0.2 and -0.5 for favourable and adverse pressure gradients, respectively, at least up to station 4 where $\partial p/\partial x$ has not yet changed sign. After the change from adverse to favourable pressure gradient on line (U) (see figure 7), history effects

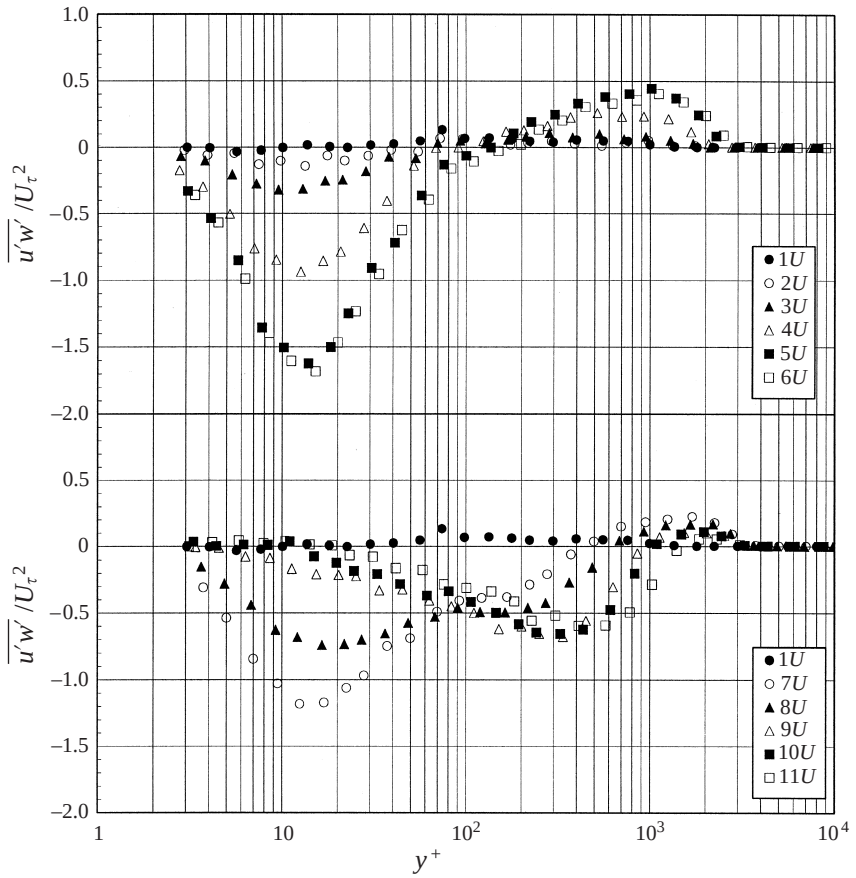

FIGURE 23. Profiles of the Reynolds shear-stress $\bar{\rho}\,\overline{u'w'}$ (ESCS) in inner-law scaling along line (U).

become, however, evident as the outer minimum at station $6U$ is still below -0.3, for instance.

From our data it appears that the outer part of the $\overline{u'v'^2}$-profile in the first bend is therefore mostly affected by the streamwise pressure gradient. The question is however far from being resolved since the data of Schwarz & Bradshaw (1994) with a comparable unilateral skewing but with an approximately zero streamwise pressure gradient show an increase of the outer peak magnitude with increasing skew angle by about a factor of two and a change of sign from negative to positive in the outer region.

In the flow region where bilateral skewing occurs (from station 7 on downstream), the profiles behave qualitatively similarly to those in the upstream region with, however, some marked differences: The approximate self-similarity near the wall is considerably degraded, especially on line (D). Second, the outer minimum moves out to $y^+ \approx 2000$ but the values of $\overline{u'v'^2}$ are very different on lines (U) and (D) (-0.25 and -0.5, respectively), indicating a correlation with the degree of cross-over in the velocity profiles (stronger on D than on U). Another curious difference between lines (U) and (D) is the appearance of triple minima (including the minimum at $y^+ < 30$) at stations $8U$ to $10U$ which, as far as we can see, can only be attributed to the different streamwise pressure gradient histories.

Like any cross-correlation containing an uneven power of w', the $\overline{v'^2w'}$ distribution

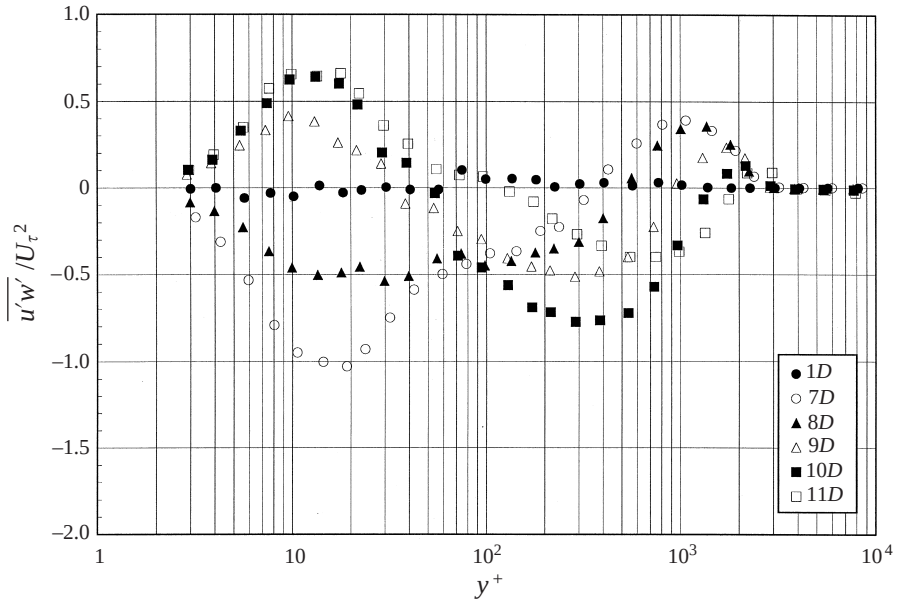

FIGURE 24. Profiles of the Reynolds shear stress $\bar{\rho}\,\overline{u'w'}$ (ESCS) in inner-law scaling along line (*D*).

(see also the $\overline{v'w'}$-profiles in figure 22) starts out as nominally zero in the upstream two dimensional part. With growing unilateral skewing of the boundary layer, the profiles develop a small negative peak in the outer region and a positive peak near the wall (figure 28) which cannot be resolved since the THWP cannot reach $y^+ < 30$ and errors of the THWP increase considerably below $y^+ \approx 50$. It is however possible to discern a correlation between the values of $\overline{v'^2w'}$ and the amount of crossflow, in agreement with the increase of $\overline{v'w'}$ (see figure 22) and with the measurements of Schwarz & Bradshaw (1994). For the profiles of $\overline{v'^2w'}$ in the cross-over region the same behaviour as for $\overline{v'w'}$ is observed.

Schwarz & Bradshaw (1994) defined a vertical transport velocity for the fluctuating kinetic energy $\overline{q'^2}$:

$$V_{q^2} = \overline{v'q'^2}/\overline{q'^2}, \tag{4.2}$$

where $\overline{v'q'^2} = \overline{u'^2v'} + \overline{v'^3} + \overline{v'w'^2}$.

Figure 29 shows that $\overline{q'^2}$ was generally transported away from the wall by v' with a large peak of V_{q^2}/U_τ in the outer region and a smaller one near the wall. The outer peak is in qualitative agreement with the data of Schwarz & Bradshaw but the trend with growing crossflow is opposite. In the present case the transport is diminished which could be explained by the effect of the favourable pressure gradient being stronger than the increase due to the growing crossflow in a boundary layer with zero streamwise pressure gradient. In the log-region the vertical transport reverses direction in the Schwarz & Bradshaw (1994) experiment which is consistent with a gradient-diffusion-like transport but is not observed in our data.

4.5. *The two-point correlation coefficient* R_{uu}

An impression of the behaviour of the large-energy-containing eddies due to crossflow may be obtained from two-point correlations. Two-point correlations have been

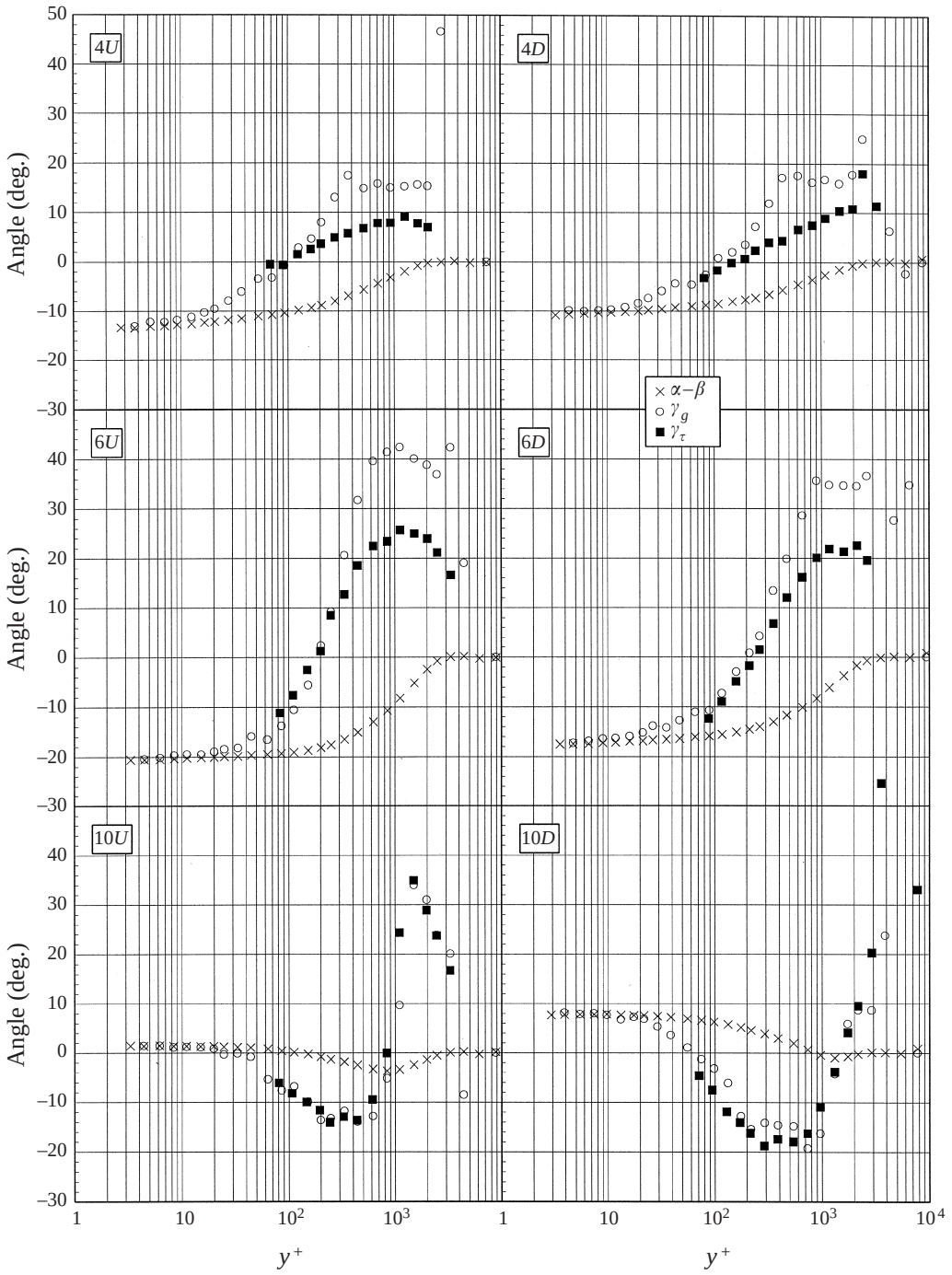

FIGURE 25. Profiles of the angles of the mean velocity $(\alpha - \beta)$ of the velocity gradient γ_g and of the shear stress vector γ_τ in inner-law scaling at three stations on the lines (U) and (D).

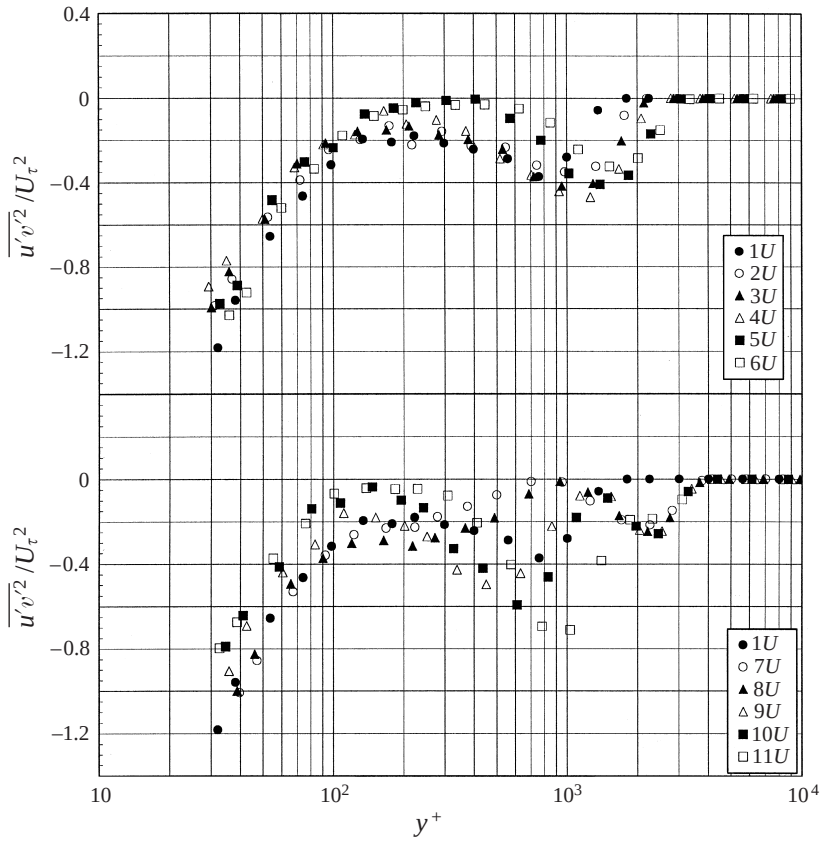

FIGURE 26. Profiles of $\overline{u'v'^2}$ (ESCS) in inner-law scaling on line (U).

measured for all three components of the fluctuating velocities by Littell & Eaton (1994) on a rotating disk. In our study, satisfactory results were obtained only for the two-point correlation coefficient R_{uu}, not presented in Littell & Eaton (1994), which was measured between the WHWP positioned 0.33 mm above the wall and a SHWP probe which was traversed to 209 stations in the (y, z)-plane with a denser spacing close to the fixed probe. It is noted that both probes were everywhere aligned with the *local* mean flow direction to minimize probe interference effects, i.e the indices of R_{uu} should be interpreted as $(\overline{u'^2} + \overline{w'^2})^{1/2}$. For other two-point correlations our multi-wire probes, despite their miniaturization, could not be moved close enough together to obtain meaningful results.

In the following, R_{uu} as defined above is presented in the (y, z)-plane at three positions characteristic of zero ($1M$), unilateral ($6M$) and bilateral ($10M$) skewing. Figure 30(a) shows the almost symmetric distribution of R_{uu} at station $1M$ with asymmetries appearing only in the contours of very small correlation. The effect of the spanwise pressure gradient on the structures is clearly visible at station $6M$ (figure 30b) where the contours are tilted in the direction of negative spanwise pressure gradient. This is in agreement with the near-wall calculations of Sendstad & Moin (1992, their figure 4.43) and with Littell & Eaton (1994). Since the boundary layer has a thickness of 70 mm at this position, we see only the inner third of the layer and here the strongest deflections are at about $y = 7$ mm which would be equivalent

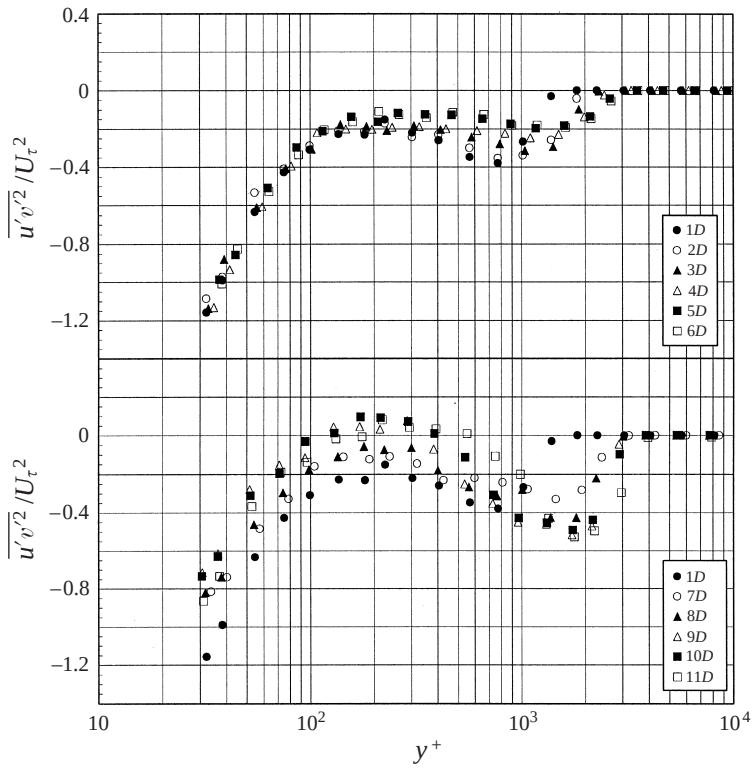

FIGURE 27. Profiles of $\overline{u'v'^2}$ (ESCS) in inner-law scaling on line (D).

to $y/\delta = 0.10$. At position $10M$ (figure 30c) where bilateral skewing occurs, the asymmetry of the R_{uu}-pattern has started to shift to the opposite side, in agreement with the change of sign of the transverse pressure gradient.

These measurements represent further evidence of the structural modifications brought about by three-dimensionality. Interestingly, at all three stations of figure 30 the initial steep decrease of R_{uu} from unity to values around $\frac{1}{3}$ is seen to be unaffected by three-dimensionality, while the tails $R_{uu} \leqslant 0.3$ are significantly affected. This can be quantified if R_{uu} along any ray emanating from the location of the fixed WHWP is represented as a superposition of a fast-decaying part $R_{uu,fast}$ and a slowly decaying part $R_{uu,slow}$ (with $\max(R_{uu,slow}) \approx \frac{1}{3}$), which may be associated with a short and a long integral length scale, respectively. The short scale associated with $R_{uu,fast}$ is $\Lambda^+_{short} = O(50)$, essentially independent of the measuring location and the direction in the (y, z)-plane. The long scale on the other hand, associated with $R_{uu,slow}$, is estimated to be $\Lambda^+_{long} = O(500)$ along the y-direction and varies little between the three stations. Along 45° lines in the (y, z)-plane, the 'long' integral scale is $\Lambda^+_{long} = O(250)$ at station $1M$ and remains approximately the same at $6M$ on the side of increasing z. However, on the side of decreasing z a clear increase to $\Lambda^+_{long} = O(500)$ is observed at $6M$. The different behaviour of the two parts of R_{uu} is consistent with the spectra of Bruns (1998), which show an influence of three-dimensionality only at low frequencies, but it appears premature to advance a physical interpretation for the observed behaviour of the two-point correlation.

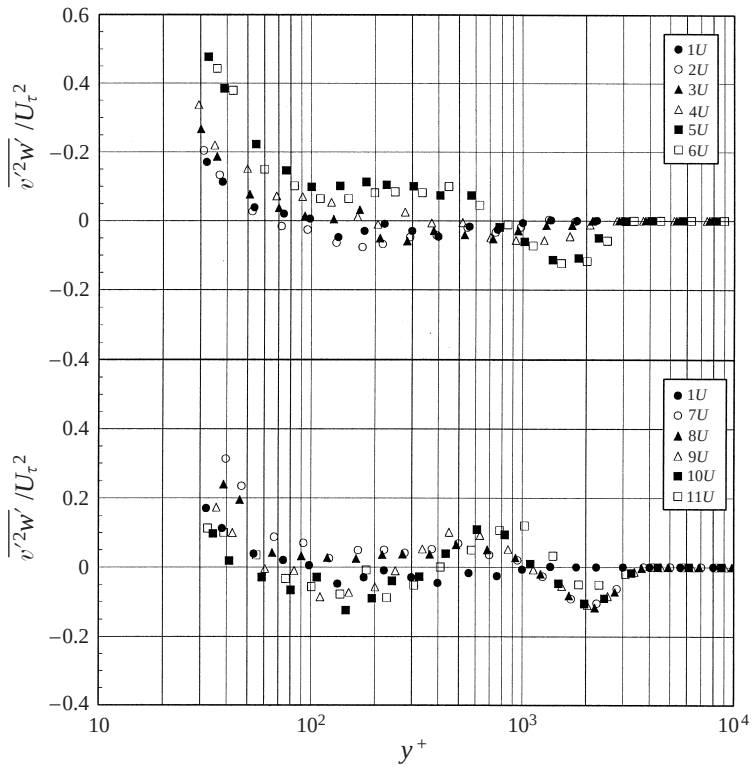

FIGURE 28. Profiles of $\overline{v'^2w'}$ (ESCS) in inner-law scaling on line (U).

4.6. *Reynolds stress transport*

The following discussion of the equation for the turbulent kinetic energy transport (TKE) at four characteristic stations will elucidate the streamwise changes in the energy budget (see Bruns 1998 for the evaluation of the other equations). The stations chosen are $1M$ where the boundary layer is two-dimensional and where $\partial p/\partial x = 0$, $3M$ with unilateral skewing and $\partial p/\partial x = 0$, $6M$ with unilateral skewing and $\partial p/\partial x < 0$, and $10M$ with bilateral skewing and $\partial p/\partial x > 0$.

All terms in the TKE-equation are evaluated in the local external streamline coordinate system. Spatial derivatives were calculated by finite differences from three smoothed experimental profiles (for details see Bruns 1998).

The terms in the TKE-equation, given for example by Hinze (1975), that were accessible to our measurements were evaluated individually, while the terms that could not be determined were lumped into the balance term

$$\text{Balance} = \nu\left[\overline{\frac{\partial u_i'}{\partial x_j}\frac{\partial u_i'}{\partial x_j}} + \frac{\partial^2 \overline{u_i'u_j'}}{\partial x_i \partial x_j}\right] - \frac{1}{\rho}\left[\frac{\partial \overline{p'u'}}{\partial x} + \frac{\partial \overline{p'v'}}{\partial y} + \frac{\partial \overline{p'w'}}{\partial z}\right] - \nu\frac{\partial^2 \overline{u_i'u_j'}}{\partial x_i \partial x_j}, \qquad (4.3)$$

which was computed from the TKE-equation. Since the dissipation contributes most to this balance term it is labelled 'dissipation' in figure 31. In agreement with Chesnakas & Simpson (1996) we find that the energy budget throughout the 3DTBL is dominated by the production and dissipation terms (note the change in scale beyond 5). A comparison of the data in the two-dimensional ZPG part of the boundary layer (station $1M$) shows good agreement with the DNS data of Spalart (1988), thus

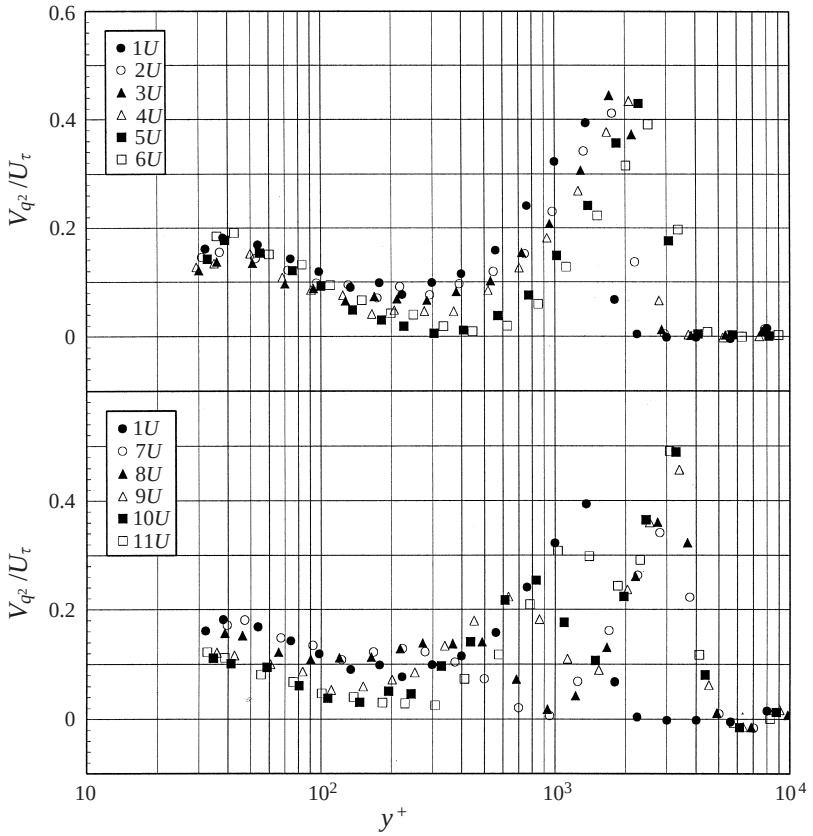

FIGURE 29. V_{q^2}/U_τ profiles along line (U).

establishing confidence in the evaluation procedure (see Bruns 1998). As a sort of calibration standard for the four graphs in figure 31, the rate of dissipation ε was approximated by $U_\tau^3/\kappa y$ ($\kappa = 0.40$ being the Kármán constant) for the two-dimensional boundary-layer profile and added to the figures as solid line.

Here, a general comment is in order. The measurements of Compton & Eaton (1995) and Chesnakas & Simpson (1996) show that the maximum of the production term non-dimensionalized by ν/U_τ^4 lies at $y^+ \approx 15$ and has a value of 0.8 and 0.28, respectively. Since our last measuring station is at $y^+ = 40$, we can only estimate this maximum. As the peak of the production profile corresponds closely to that of the Reynolds normal stress $\overline{\rho}\,\overline{u'^2}$, $y^+ \approx 15$ is consistent with figure 15 and also agrees with measurements of the production term in a favourable- and zero-pressure-gradient boundary layer by Fernholz & Warnack (1998) and Fernholz & Finley (1996), respectively. The maximum of the principal production term $[(\overline{u'v'}\partial U/\partial y)\nu/U_\tau^4]$, on the other hand, can be estimated from figure 15 to be about 0.28 which corresponds to the maximum measured by Chesnakas & Simpson (1996). It is also consistent with the maximum value of 0.25 of the principal production term $[(\overline{u'v'}\partial U/\partial y)\nu/U_\tau^4]$ calculated by Rotta (1962) for a two-dimensional ZPG boundary layer, as the additional production term $[(\overline{u'v'}\partial W/\partial y)\nu/U_\tau^4]$ in a 3DTBL is expected to only moderately increase production.

Since our data do not extend close enough to the wall, although they extend closer to the wall than earlier hot-wire measurements, a detailed discussion, as for example

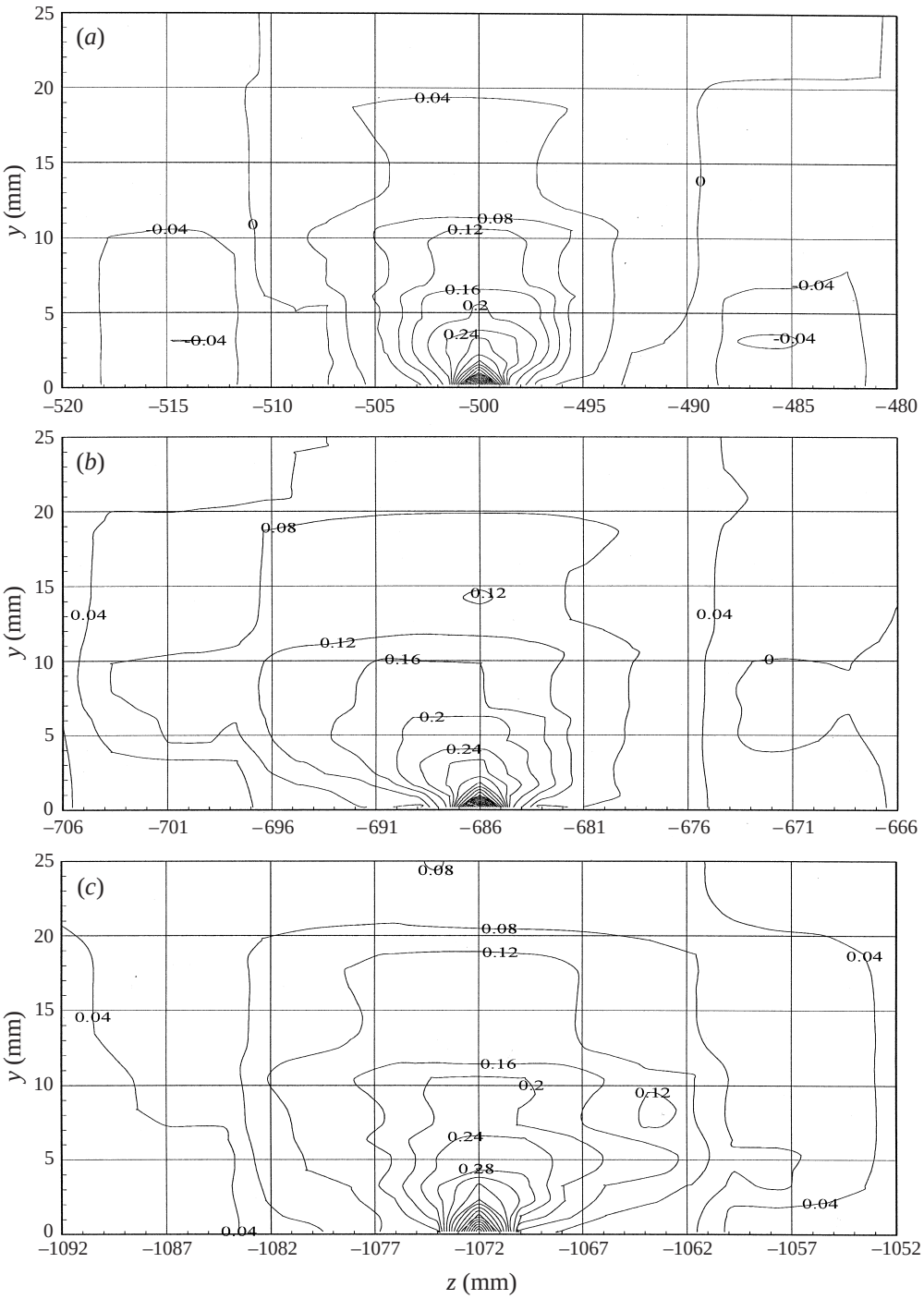

FIGURE 30. Iso-contours of the two-point correlation coefficient R_{uu}, where u is in the direction of the local streamline, in the (y, z)-plane at stations (*a*) $1M$, (*b*) $6M$ and (*c*) $10M$.

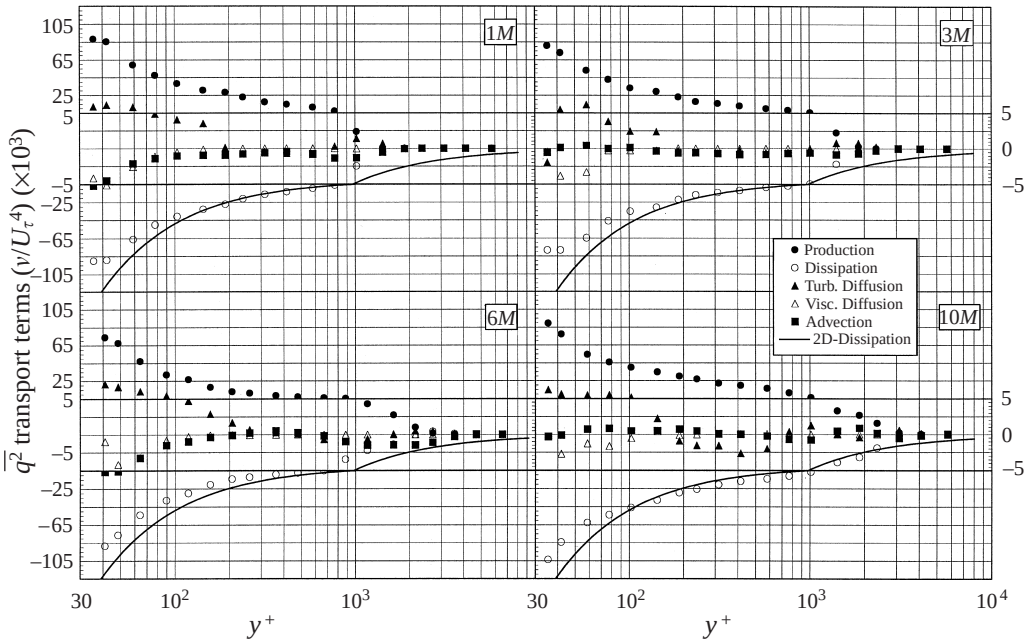

FIGURE 31. Budget of the turbulent kinetic energy in inner scaling at stations $1M$, $3M$, $6M$ and $10M$ (note the different scale for $-5 \leqslant y \leqslant +5$).

in Schwarz & Bradshaw (1994), is not appropriate. The one preliminary conclusion which can however be drawn is that production and dissipation decrease slightly with increasing skewing of the boundary layer ($6M$) and increase at the cross-over station ($10M$). The dissipation term at $10M$ is balanced by the production and by the turbulent diffusion which peaks at about $y^+ = 400$. The increase of the turbulent diffusion term results mainly from larger values of the triple products $\overline{u'^2v'}, \overline{v'^3}$ and $\overline{v'w'^2}$ entailing larger gradients in the vertical direction (for details see Bruns 1998). Similar conclusions hold for the terms of the Reynolds stress transport equations (see Bruns 1998).

5. Discussion of local non-equilibrium and conclusions

The measurements of Bruns (1998) were performed with the goal of obtaining, by means of hot-wire probes, a complete set of turbulence data as close to the wall as possible which could serve to further elucidate their evolution as a function of spanwise and streamwise pressure gradients. In this paper we have presented a selection of these data for which we can offer some interpretation or speculation. For a wealth of other data, in particular data for all the measuring stations of figure 3, different measures of the boundary layer thickness, integral length scales, higher statistics of u' and a discussion of the Reynolds stress transport equations the reader is referred to Bruns (1998). Furthermore it is planned to make the original data available on the website http://lmfwww.epfl.ch/lmf/.

The first general conclusion concerns some open problems of near-wall measurements in presssure-driven 3DTBLs with unilateral and bilateral skewing. To simultaneously measure all three components of the instantaneous velocity at a large number of points, the most economical solution is a triple hot-wire probe. Since no

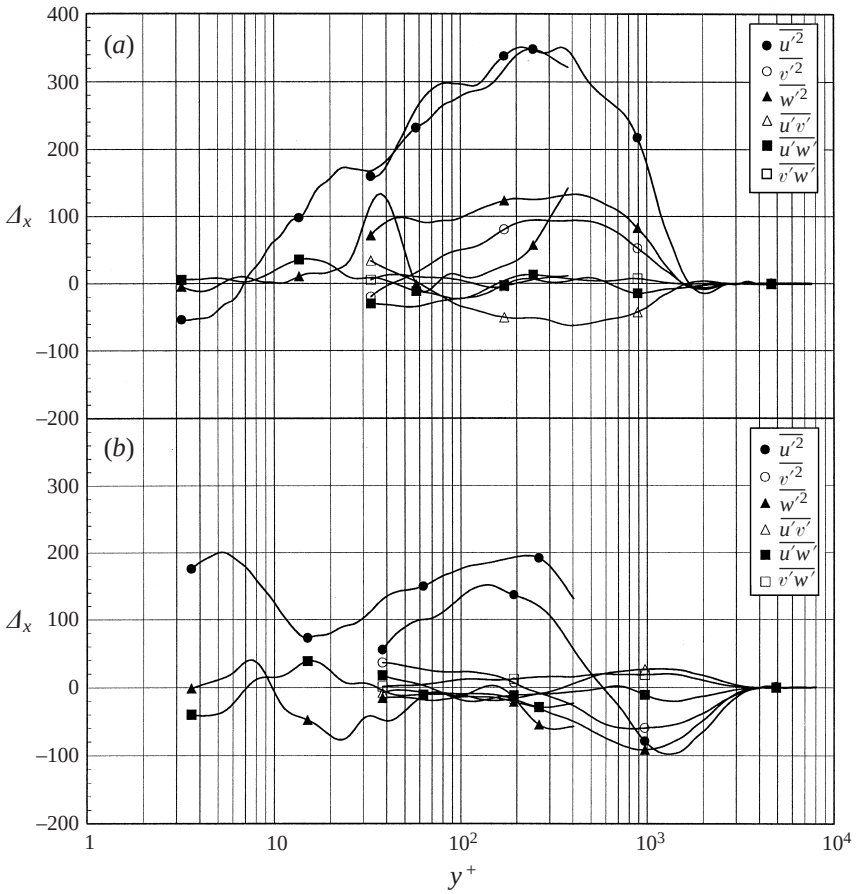

FIGURE 32. Non-dimensional function $\Delta_x S(y^+)$ for the six Reynolds stresses S as determined (*a*) from the stations $3U$–$3D$ and (*b*) from the stations $6U$–$6D$.

miniature probe of this type was commercially available, a probe had to be designed, manufactured and tested. Owing to the limits of probe size the region between the wall and $y^+ \approx 40$ was however only accessible to single-wire probes in our study with prongs traversed through the test plate. We believe that with the development of these specialized hot-wire probes, their application in TBLs has now more or less reached its limits. Further progress seems possible only with highly focused laser beams in the manner of Ölçmen & Simpson (1995*a*) and Chesnakas & Simpson (1996) or by direct numerical simulation (e.g. Sendstad & Moin 1992). Having experienced at first hand some of the problems associated with measurements in the immediate vicinity of the wall, we believe that the quality of the different measuring techniques will finally have to be decided by DNS (see e.g. the data of Compton & Eaton 1995, and the DNS of Sendstad & Moin 1992).

Next we make a comment on the history effects that have been invoked throughout this text to 'explain' discrepances between expected (on the basis of some simplified idea) and actually measured profiles. It is clear that history effects are in principle accounted for by appropriate Reynolds stress transport models. However, the associated closure hypotheses typically involve assumptions of local equilibrium in some form, e.g. local 'diffusivities' and redistribution mechanisms of Reynolds stresses.

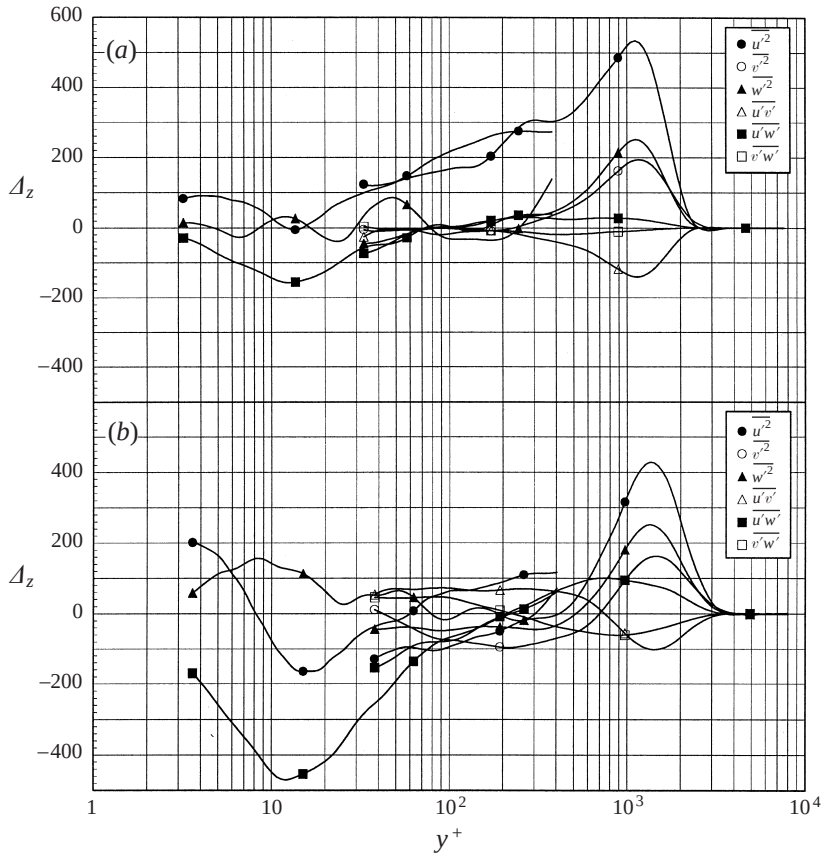

FIGURE 33. Non-dimensional function $\Delta_z S(y^+)$ for the six Reynolds stresses S as determined (a) from the stations $3U$–$3D$ and (b) from the stations $6U$–$6D$.

In particular, local equilibrium of turbulence is believed to prevail in a wall layer below, say, $y^+ \approx 50$. This wall layer has also been the object of low-dimensional dynamical models for turbulence-sustaining cycles involving the principal coherent near-wall structures (streaks, streamwise vortices) and their instabilities (see e.g. Jiménez & Pinelli 1999). To tackle the question of their possible 'universality', it is again of interest to investigate whether the turbulence reaches local equilibrium for $y^+ \leqslant 50$ in the present three-dimensional turbulent boundary layer. If it does not, the chances of formulating any 'universal' model of the wall cycle are clearly compromised.

To advance this discussion, an attempt is made to quantify the degree of local equilibrium in the present boundary layer. To this end, we assume that the Reynolds stress profiles are fully determined by local quantities, i.e. by the local U_τ and the local pressure gradients. Furthermore we concentrate on the inner part of the Reynolds stress profiles in inner-law scaling and their deviations from ZPG-profiles. Under these assumptions, any stress component $S_{(i)}$ at a measuring location (i) can be expanded in a double Taylor series with respect to the two non-dimensional pressure gradients. Working in the external streamline coordinate system (ESCS) and truncating the series at linear order, which seems appropriate for the weak to moderate pressure

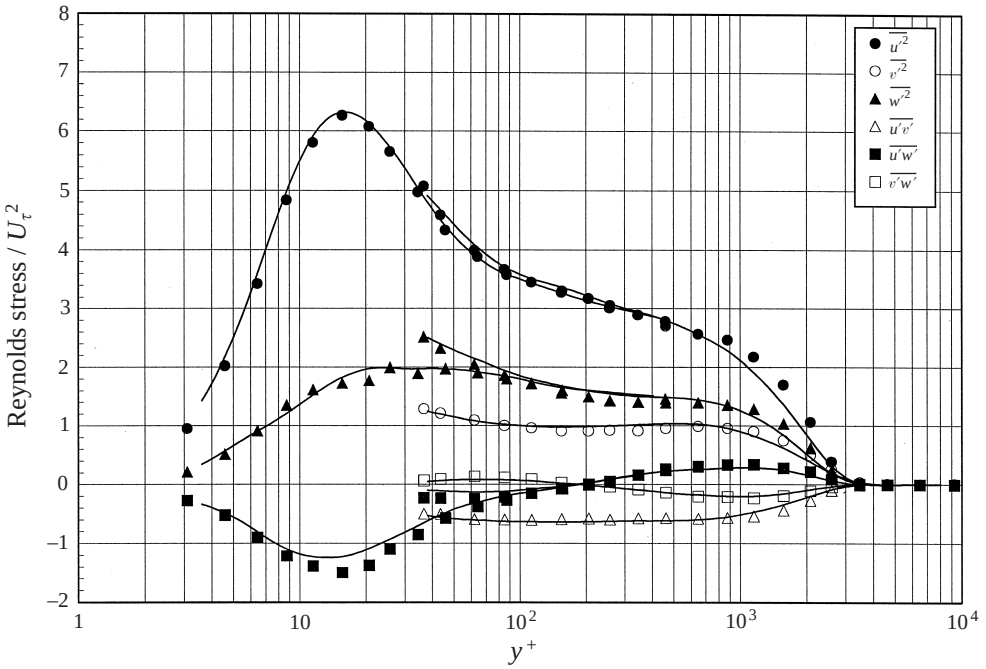

FIGURE 34. Measured Reynolds stress profiles at station $6M$ (symbols) and profiles interpolated from data at stations $6U$ and $6D$ (solid lines).

gradients of our experiment, one can approximate

$$S_{(i)}(y^+;\Pi_x^{(ESCS)},\Pi_z^{(ESCS)}) - S_{(1M)}(y^+;0,0) = \Pi_{x,(i)}^{(ESCS)}\Delta_x S(y^+) + \Pi_{z,(i)}^{(ESCS)}\Delta_z S(y^+) + O(\Pi^2), \tag{5.1}$$

where the profiles at station $1M$ are taken as two-dimensional ZPG reference profiles, $\Pi_{\bullet,(i)}^{(ESCS)} = (\nu/\rho U_\tau^3)\partial p/\partial \bullet$ are the non-dimensional pressure gradients in external streamline coordinates at station (i), and $\Delta_x S(y^+)$ and $\Delta_z S(y^+)$ must be *universal* functions associated with the quantity S. These functions can be determined by solving a system of two of the above equations corresponding to different stations (i) with different $\partial p/\partial x$ and $\partial p/\partial z$. In practice, this is carried out after smoothing the profiles with a 100-point quadratic Spline fit and a low-pass filter. Examples of these functions, determined from the station pairs $3U$–$3D$ and $6U$–$6D$ are shown as figures 32 and 33 for the six Reynolds stresses. For three of the components, both data from the THWP (down to $y^+ = 30$) and from the SHWP (down to $y^+ = 3$) have been used which give an impression of the measurement error in the overlap region of the two probes.

From figures 32 and 33 it is obvious that the two functions Δ are far from universal over the entire boundary layer thickness all the way down to the last available point at $y^+ = 3$ (note that even the sign of $\Delta_{x,\overline{u'^2}}(y^+ = 3)$ is different on figures 32(a) and 32(b)). From this it must be concluded that, even for our moderate pressure gradients, the boundary layer under investigation is clearly out of equilibrium all the way into the viscous sublayer.

It is noteworthy that, despite the non-universality of the functions Δ, the above local Taylor expansion provides interpolated profiles of a surprising quality for

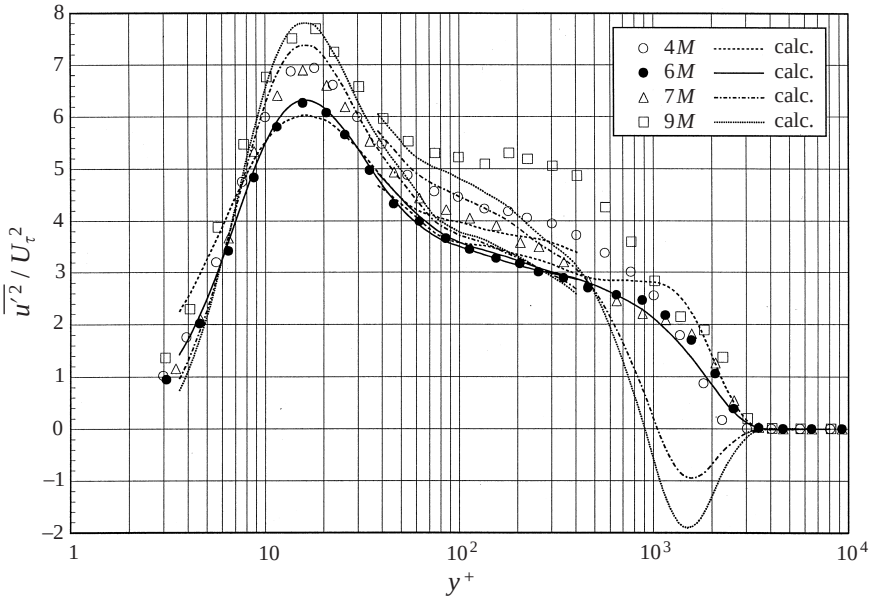

FIGURE 35. Comparison of measured non-dimensional $\overline{u'^2}$-profiles along line (M) (symbols) with profiles predicted (curves) on the basis of Δ determined from the stations $6U$–$6D$.

nearby stations. An example is given in figure 34 where all Reynolds stress profiles are reproduced within measurement accuracy by (5.1) where the Δ-functions have been determined from the nearby pair ($6U$–$6D$). Again, the measurement error can be assessed in the overlap region of the SHWP and the THWP.

However, when using the 'local equilibrium hypothesis' to reproduce profiles further away from the reference stations, the results are disastrous, as shown for the example of $\overline{u'^2}$ and $\overline{u'w'}$ on figures 35 and 36, respectively. Note that in these two figures we have also included the station $4M$, which is located upstream of the reference stations $6U$ and $6D$, since (5.1) should be valid for any combination of stations if the underlying 'local equilibrium hypothesis' holds. The corresponding 'predictions' of $\overline{u'v'}$ (not shown for brevity's sake) by (5.1) are just as bad. In fact, for most of the non-diagonal Reynolds stress components the ZPG-profile is a much better approximation than the profile obtained from (5.1)!

These last figures make it amply clear that the 'local equilibrium hypothesis' is inappropriate over the *entire* thickness of the boundary layer. In other words, we must conclude that a turbulence model based on some form of local equilibrium assumptions has probably little chance of consistently describing real turbulence in complex 3DTBLs. Besides this general conclusion, figures 34 to 36 also allow the specific and potentially useful conclusion that different histories of weak to moderate streamwise pressure gradients apparently have little effect on the profiles (see the excellent fit in figure 34), while different histories of the spanwise pressure gradient seem to have a much stronger effect on the degree of non-equilibrium (see the effect of sign changes of $\partial p/\partial z$ on the fits of figures 35 and 36). The reader is however warned that stronger streamwise pressure gradient variations do perturb equilibrium significantly, as our 'local equilibrium hypothesis' has also failed in the strongly decelerated and accelerated two-dimensional boundary layers of Dengel & Fernholz (1990) and Fernholz & Warnack (1998), respectively.

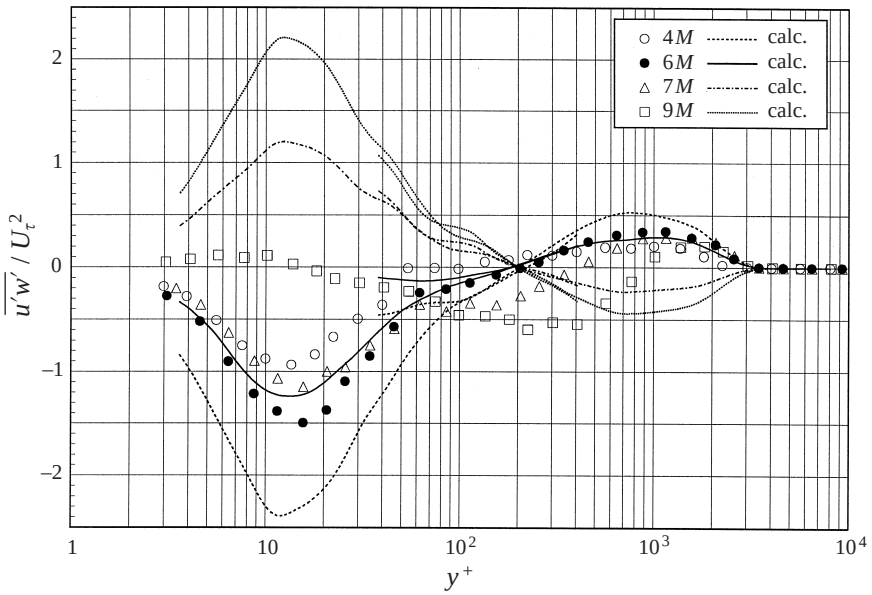

FIGURE 36. Comparison of measured non-dimensional $\overline{u'w'}$-profiles along line (M) (symbols) with profiles predicted (curves) on the basis of Δ determined from the stations $6U$–$6D$.

Finally, we would like to re-emphasize that the interpretation of the present data, being among the first near-wall turbulence data in a region of bilaterally skewed cross-flow profiles, are certainly not definitive. We hope that they will stimulate further analysis and comparisons with direct simulations of 3DTBLs and with turbulence models.

This investigation owes much to the generous support and symphathy of I. L. Ryhming. The first author acknowledges the finacial support of the Deutsche Forschungsgemeinschaft (DFG) and of COST F1 through a grant from the Swiss Federal Office of Education and Science.

The triple-wire probe would not exist without the patience and skill of A. Ebner and the whole research project has much benefited over the years from the assistance and advice of T. V. Truong.

REFERENCES

ALVING, A. & FERNHOLZ, H. H. 1996 Turbulence measurements around a mild separation bubble and downstream of reattachment. *J. Fluid Mech.* **322**, 297–328.

BRUNS, J. 1998 Experimental investigation of a three-dimensional turbulent boundary layer in an '*S*'-shaped duct. Dissertation TU Berlin (D83).

BRUNS, J. M. & DENGEL, P. 1998 A miniature triple hot-wire probe for wall bounded flows. *Exps. Fluids* **24**, 479–488.

CHESNAKAS, C. J. & SIMPSON, R. L. 1996 Measurments of the turbulence structure in the vicinity of a three-dimensional separation. *Trans. ASME* I: *J. Fluid Engng* **118**, 268–275.

CHESNAKAS, C. J., SIMPSON, R. L. & MADDEN, M. M. 1994 Three-dimensional velocity measurements on a 6 : 1 prolate spheroid at 10° angle of attack. *Data Rep.* VLPI-AOE-202. Dept. Aerospace and Ocean Eng. VPI Blacksburg, VA.

COMPTON, D. A. & EATON, J. D. 1995 Near-wall measurements of three-dimensional turbulent boundary layer. *Thermosciences Division Rep.* MD-72. Dept. of Mechanical Engineering, Stanford University.

Cousteix, J. 1986 Three-dimensional and unsteady boundary layer computations. *Ann. Rev. Fluid Mech.* **18**, 173–196.

Dengel, P. & Fernholz, H. H. 1990 An experimental investigation of an incompressible turbulent boundary layer in the vicinity of separation. *J. Fluid Mech.* **212**, 615–636.

Dengel, P., Fernholz, H. H. & Vagt, J.-D. 1981 Turbulent and mean flow measurements in an incompressible axisymmetric boundary layer with incipient separation. *Turbulent Shear Flows*, vol. 3, pp. 225–236. Springer.

Eaton, J. K. 1995 Effects of mean flow three-dimenionality on turbulent boundary-layer structure. *AIAA J.* **33**, 2020–2025.

Eichelbrenner, E. A. 1963 Theoretical investigation and control by measuring tests on the behaviour of the three-dimensional turbulent boundary layer on an annular wing at various incidences. Bureau Technique Zborowski, Brunoi (available as AD 428 671).

Eichelbrenner, E. A. 1973 Three-dimensional boundary layers. *Ann. Rev. Fluid Mech.* **5**, 339–361.

Eichelbrenner, E. A. & Peube, J.-L. 1966 The role of '*S*'-shaped crossflow profiles in three-dimensional boundary layer theory. *Final Rep. Contract* N 62558-4460, Faculté des Sciences de Poitier (available as AD 650 953).

Erm, L. P. 1988 Low Reynolds-number turbulent boundary layers. PhD thesis, University of Melbourne.

Fernholz, H. H. & Finley, P. J. 1996 The incompressible zero-pressure-gradient turbulent boundary layer: An assessment of the data. *Prog. Aerospace Sci.* **32**, 245–311.

Fernholz, H. H., Janke, G., Schober, M., Wagner, P. M. & Warnack, D. 1996 New developments and applications of skin-friction measuring techniques. *Meas. Sci. Technol.* **7**, 1396–1409.

Fernholz, H. H. & Warnack, D. 1998 The effects of a favourable pressure gradient and of the Reynolds number on an incompressible axisymmetric turbulent boundary layer. Part 1. The turbulent boundary layer. *J. Fluid Mech.* **359**, 329–356.

Goldberg, U. & Reshotko, E. 1984 Scaling and modeling of three-dimensional pressure-driven turbulent boundary layer. *AIAA J.* **22**, 914–920.

Gruschwitz, E. 1935 Turbulente Reibungsschichten mit Sekundärströmung. *Ing.-Arch.* **6**, 355–365.

Hawthorne, W. R. 1951 Secondary circulation in fluid flow. *Proc. R. Soc. Lond.* A **206**, 374–386.

Hinze, J. O. 1975 *Turbulence*, 2nd Edn. McGraw-Hill.

Jiménez, J. & Pinelli, A. 1999 The autonomous cycle of near-wall turbulence. *J. Fluid Mech.* **389**, 335–359.

Johnston, J. P. 1960 On the three-dimensional turbulent boundary layer generated by secondary flow. *Trans. ASME* D: *J. Basic Engng* March 1960, 233–246.

Johnston, J. P. 1976 Experimental studies in three-dimensional turbulent boundary layers. *Thermosci. Div. Rep.* MD-34. Dept. of Mechanical Engineering, Stanford University.

Johnston, J. P. & Flack, K. A. 1996 Review – advances in three-dimensional turbulent boundary layers with emphasis on the wall-layer regions. *Trans. ASME* I: *J. Fluid Engng* **118**, 219–232.

Klinksiek, W. F. & Pierce, F. J. 1970 Simultaneous lateral skewing in a three-dimensional turbulent boundary layer flow. *Trans. ASME* D: *J. Basic Engng* **92**, 83–92.

Klinksiek, W. F. & Pierce, F. J. 1973 A finite difference solution of the two- and three-dimensional incompressible turbulent boundary-layer equations. *J. Fluid Mech.* **95**, 445–458.

Littell, H. S. & Eaton, J. K. 1994 Turbulence characteristics of the boundary layer on a rotating disk. *J. Fluid Mech.* **266**, 175–207.

Murliss, J., Tsai, H. M. & Bradshaw, P. 1982 The structure of turbulent boundary layers at low Reynolds numbers. *J. Fluid Mech.* **122**, 13–56.

Ölçmen, S. M. & Simpson, R. L. 1992 Perspective: On the near-wall similarity of three-dimensional turbulent boundary layers. *Trans. ASME* I: *J. Fluid Engng* **114**, 487–495.

Ölçmen, S. M. & Simpson, R. L. 1995*a* A five-velocity-component laser-doppler velocimeter for measurements of a three-dimensional turbulent boundary layer. *Meas. Sci. Technol.* **6**, 702–716.

Ölçmen, S. M. & Simpson, R. L. 1995*b* An experimental study of a three-dimensional pressure-driven turbulent boundary layer. *J. Fluid Mech.* **290**, 225–262.

Ölçmen, S. M. & Simpson, R. L. 1996 An experimental study of a three-dimensional pressure-driven turbulent boundary layer. *Trans. ASME* I: *J. Fluid Engng* **118**, 416–418.

Österlund, J. M. & Johansson, A. V. 1995 Dynamic behaviour of hot-wire probes in turbulent boundary layers. *Proc. ETC-5*, *Sienna*, pp. 398–402. Kluwer.

PARKER, R. D. 1994 Boundary layer calculations of the S-duct, Pt.1. *Internal Rep.* T-94-29. IMHEF, EPFLausanne.

PARKER, R. D. & BRUNS, J. M. 1996 Anisotropic turbulence modeling in a complex three-dimensional boundary layer flow. *Comput. Fluid Dyn. 96: Proc. 3rd ECCOMAS Comp. Fluid Dynamics Conf., Paris*, pp. 146–152. Wiley.

PARNEIX, S. & DURBIN, P. 1997 Numerical simulation of three-dimensional turbulent boundary layers using the V2F model. *CTR Ann. Res. Briefs*, pp. 135–148.

PIERCE, F. J. & EAST, J. L. 1972 Near-wall collateral flow in three-dimensional turbulent boundary layers. *AIAA J.* **10**, 334–336.

ROGERS, B. K. & HEAD, M. R. 1969 Measurment of three-dimensional boundary layers. *J. R. Aero. Soc.* **73**, 796–798.

ROTTA, J. C. 1962 Turbulent boundary layers in incompressible flow. *Progr. Aeronaut Sci.* **2**, 5–219.

RYHMING, I. L., TRUONG, T. V. & LINDBERG, P. A. 1992 Summary and conclusions for test-case T1, numerical simulation of unsteady flows and transition to turbulence. *Proc. ERCOFTAC Workshop, EPFL, 28. March 1990, Lausanne, Switzerland* (ed. O. Pironneau, W. Rodi, I. L. Rhyming, A. M. Savill, T. V. Truong), pp. 197–243. Cambridge University Press.

SCHWARZ, W. R. & BRADSHAW, P. 1992 Three-dimensional turbulent boundary layer in a 30 degree bend: Experiment and Modeling. *Thermosci. Div. Rep.* MC-61, Dept. of Mechanical Engineerin, Stanford University.

SCHWARZ, W. R. & BRADSHAW, P. 1993 Measurements in a pressure-driven three-dimensional turbulent boundary layer during development and decay. *AIAA J.* **31**, 1207–1214.

SCHWARZ, W. R. & BRADSHAW, P. 1994 Turbulence structural changes for a three-dimensional turbulent boundary layer in a 30° bend. *J. Fluid Mech.* **272**, 183–209.

SENDSTAD, O. & MOIN, P. 1992 The near-wall mechanics of three-dimensional boundary layers. *Thermosci. Div. Rep.* TF-57, Dept. of Mechanical Engineering, Stanford University.

SHANEBROOK, J. R. & HATCH, D. E. 1970 Discussion of the paper by W. F. Klinksiek & F. J. Pierce. *Trans. ASME* D: *J. Basic Engng* **92**, 90–91.

SPALART, P. R. 1988 Direct simulation of a turbulent boundary layer up to $R_\theta = 1410$. *J. Fluid Mech.* **187**, 61–98.

SQUIRE, H. B. & WINTER, K. G. 1951 The secondary flow in a cascade of airfoils in a nonuniform stream. *J. Aero. Sci.* **18**, 271–277.

TRUONG, T. V. & BRUNET, M. 1992 Test case T1: Boundary layer in a '*S*'-shaped channel. *Proc. Ercoftac Workshop on Numerical Simulation of Unsteady Flows and Transition to Turbulence.* Cambridge University Press.

VAGT, J.-D. & FERNHOLZ, H. H. 1973 Use of surface fences to measure wall shear stress in three-dimensional boundary layers. *Aero. Q.* **24**, 87–91.

VAGT, J.-D. & FERNHOLZ, H. H. 1979 A discussion of probe effects and improved measuring techniques in the near-wall region of an imcompressible three-dimensional turbulent boundary layer. *AGARD Conf. Proc.* 271, pp. 10.1–10.17.

WAGNER, P. M. 1991 The use of near-wall hot-wire probes for time-resolved skin-friction measurements. *Advances in Turbulence* vol. 3, pp. 524–529. Springer.

WARNACK, D. 1996 Eine experimentelle Untersuchung bescheunigter turbulenter Wandgrenzschichten. Dissertation TU Berlin (D 83).

WEBSTER, D. R., DEGRAAFF, D. B. & EATON, J. K. 1996 Turbulence characteristics of a boundary layer over a swept bump. *J. Fluid Mech.* **323**, 1–22.